Operating Principles of VCSELs

Rainer Michalzik and Karl Joachim Ebeling

University of Ulm, Optoelectronics Department, D-89069 Ulm, Germany

Abstract. In this chapter we will deal with major principles of vertical-cavity surface-emitting laser (VCSEL) operation. Basic device properties and generally applicable cavity design rules are introduced. The following description of emission characteristics is restricted to high efficiency VCSELs that apply selective oxidation for current and photon confinement. Both the 850 and 980 nm wavelength regions are considered. Dynamics and noise behavior are discussed in terms of the small-signal modulation response as well as the relative intensity noise. The prevailing part of the text is related to transverse singlemode VCSELs, being superior to their multimode counterparts in many respects. Applications of these devices in optical interconnects are finally described and digital data transmission at data rates up to 12.5 Gbit/s over single- and multimode silica and plastic optical fibers is reported.

1 Introduction

For some time already, VCSELs have emerged from a laboratory curiosity to an object of industrial mass production. Main applications of the devices are found today in optical interconnects, such as single channel Gigabit Ethernet or even parallel transceiver modules based on multimode fiber ribbons, where the 770 to 860 nm wavelength range has been agreed upon as a standard on the below-1 μm side of the optical spectrum[1]. This chapter is intended to provide the reader with the basic knowledge necessary to understand VC-SEL benefits and limitations and at the same time give an overview over some state-of-the-art performance data obtained experimentally. We start with basic studies of the laser cavity, such as amplification and reflector properties, where essential differences to edge-emitting laser operation are underlined. A better insight into field distributions and energy flux in the VCSEL cavity is then obtained from numerical calculations with the transfer matrix method. Power conversion efficiency is of particular interest and briefly treated separately. Concentrating on a specific kind of high performance VCSEL manufacturing, we then deal with the emission characteristics of oxide-confined devices, describing in some detail achieved operation and temperature behaviors. An intuitive understanding of transverse mode guiding effects is provided. In order to treat dynamic and noise properties, we briefly write down the laser rate equations to obtain small-signal modulation responses as well as relative intensity noise spectra. A concise subsection is devoted to the emission linewidth, basically determined by random spontaneous

[1] IEEE 802.3z Gigabit Ethernet standard, 1000BASE-SX physical layer.

emission processes. Especially with respect to noise phenomena, advantages of single compared to multi transverse mode emission become apparent. As the dominant application area of VCSELs, optical interconnects are finally discussed, where emphasis is put on fiber coupling properties, large-signal modulation effects, and high-speed optical data transmission over various types of fiber.

2 Basic Properties of VCSELs

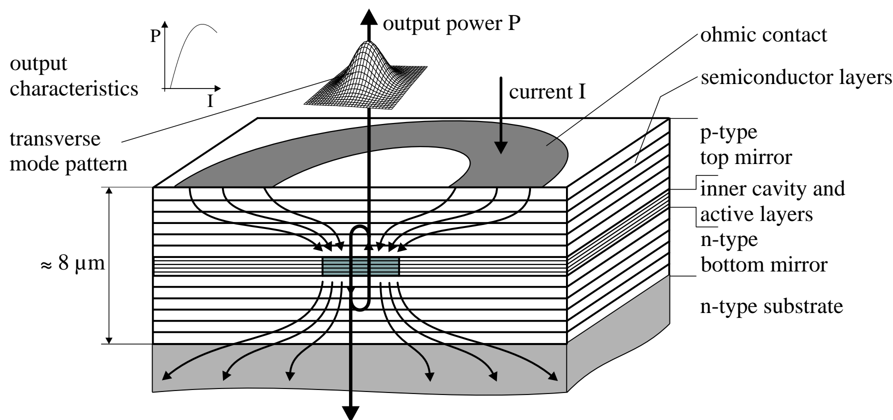

Fig. 1. Schematic layer structure and operation principle of a VCSEL

Figure 1 illustrates the typical layout of a VCSEL [1]–[3]. The inner cavity containing the amplifying layers is surrounded by electrically conductive layer stacks that form the laser mirrors which provide optical feedback. VCSELs designed for emission wavelengths in the 850 to 980 nm spectral range require about 8 µm of epitaxially grown material, whereas the active region is composed of just a few quantum wells (QWs) with some ten nm thickness. Metal organic chemical vapor deposition (MOCVD) or molecular beam epitaxy (MBE) are preferred for crystal growth. The pin-type doping configuration is similar to conventional edge-emitting lasers (EELs). In the most simple device layouts, electric current is injected from ohmic contacts on the top epitaxial side and the backside of the substrate. Several methods have been successfully employed to achieve current confinement to a predefined active area. Among those are simple mesa etching of the top mirror [4], [5], ion implantation to create highly resistive semiconductor regions [6], [7], or selective lateral oxidation [8] of a some ten nm thick semiconductor layer with high Aluminum content like $Al_{0.98}Ga_{0.02}As$ or even AlAs. Proton implantation has already been brought to perfection to fabricate commercial VCSELs

of outstanding producibility and reliability [9], [10]. On the other hand, selective oxidation introduces less optical losses in the cavity and has produced devices of unrivalled performance [11], [12]. Due to their enormous potential, in this chapter we will almost exclusively concentrate on the characteristics of oxide-confined VCSELs and explain fabrication principles below in Sect. 3.

The active diameter of the VCSEL can be reduced to just a few micrometers in order to obtain lowest threshold currents in the sub-100 µA range [13], but can also exceed 100 µm to get high output powers beyond 100 mW [14], [15]. As a rule of thumb, planar, selectively oxidized VCSELs without (internally [16] or externally [17], [18]) extended cavity emit in a single transverse mode, as indicated in Fig. 1, up to active diameters of about 4 µm. Larger devices start lasing on several higher radial and azimuthal order modes right above or even at threshold. The light-current curve has a constant slope above threshold, as common for laser diodes, but shows a characteristic rollover for higher currents due to internal heating. Unlike for EELs it is uncritical to operate VCSELs up to their maximum output powers since power densities remain in the lower $\mathrm{kW/cm^2}$ range and cannot induce optical damage to the semiconductor material or the laser facet. Depending on the wavelength and material composition, VCSELs can be designed for top emission through a ring contact or bottom emission through a transparent substrate.

2.1 Relative Confinement Factor

Figure 2 shows the layer structure and the standing-wave pattern of the electric field in the inner part of a VCSEL cavity realized in the AlGaAs material system. Calculation is done with the transfer matrix method described in Sect. 2.4. Analogously to a simple Fabry-Pérot type EEL with its mirrors composed of abrupt semiconductor-air interfaces, maxima of the electric field amplitude are found at both ends of the inner cavity of length L. With a positive integer m and the spatially averaged refractive index $\langle\bar{n}\rangle$, the resonance condition for the emission wavelength λ is then simply written as

$$\langle\bar{n}\rangle L = m\lambda/2 \; . \tag{1}$$

The active layers have to be placed in an antinode of the standing-wave pattern in order to provide good coupling between electrons and photons. Since splitting of the active region into segments separated by $\lambda/(2\langle\bar{n}\rangle)$ has to be avoided for reasons of carrier injection efficiency, the shortest symmetric cavity is just one wavelength thick, equivalent to $m = 2$.

An important difference between a VCSEL cavity and a conventional EEL cavity arises from the fact that the active gain region does not extend over the full cavity length L but is enclosed by larger bandgap layers to form a double-heterostructure. Therefore, for an arbitrary position and total thickness d_a of

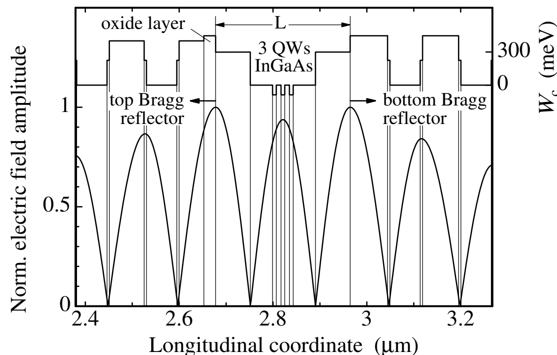

Fig. 2. Spatial distribution of the normalized electric field amplitude in the center region of a VCSEL together with the conduction band edge W_c, neglecting band bending effects. Details of the plot are discussed in connection with Fig. 6

the active layers, we have to take into account the overlap with the standing-wave pattern $E(z)$ in order to obtain the average gain in the cavity [19]. We define the relative confinement factor or gain enhancement factor by

$$\Gamma_r = \frac{L}{d_a} \frac{\int_{d_a} |E(z)|^2 \, dz}{\int_L |E(z)|^2 \, dz} , \tag{2}$$

imposing that for all further considerations the material gain coefficient g of the QWs has to be modified to $\Gamma_r g$. The electric field profile in the central $\lambda/(2\langle\bar{n}\rangle)$ part of the cavity in Fig. 2 is very well approximated by

$$E(z) = E_0 \cos(2\pi\langle\bar{n}\rangle z/\lambda) \tag{3}$$

if $z = 0$ is centered in the inner cavity, resulting in

$$\Gamma_r = 1 + \frac{\sin(2\pi\langle\bar{n}\rangle d_a/\lambda)}{2\pi\langle\bar{n}\rangle d_a/\lambda} \tag{4}$$

for a single gain segment. The gain enhancement factor of a perfectly aligned active layer is thus expressed as a raised-sinc function. For a thin QW we have $\Gamma_r \to 2$. For $d_a = m\lambda/(2\langle\bar{n}\rangle)$ we obtain $\Gamma_r = 1$, as known for EELs. In the general case of M_a active sections (usually multiple QWs) with equal gain, located at positions $z_{il} \le z \le z_{ih}$ with $i = 1, \ldots, M_a$ we find

$$\Gamma_r = 1 + \frac{\lambda}{4\pi\langle\bar{n}\rangle} \frac{\sum_{i=1}^{M_a} \sin(4\pi\langle\bar{n}\rangle z_{ih}/\lambda) - \sin(4\pi\langle\bar{n}\rangle z_{il}/\lambda)}{\sum_{i=1}^{M_a} z_{ih} - z_{il}} , \tag{5}$$

where $z = 0$ is located as before. For the VCSEL from Fig. 2 with three centered 8 nm thick QWs separated by 10 nm barriers we get $\Gamma_r = 1.8$. By exploiting the standing-wave effect, one can therefore almost double the available amount of optical amplification.

2.2 Bragg Reflectors

The VCSEL mirrors in Fig. 1 are realized as Bragg reflectors which consist of an alternating sequence of high and low refractive index layers with quarter wavelength thickness. Typically more than 20 Bragg pairs are required for each mirror. Field distributions and spectral dependencies of the reflectivity are suitably calculated by the transfer matrix method described in Sect. 2.4. Properties of Bragg reflectors are treated in more detail in an extra chapter, so that we will restrict ourselves to some basic analytical discussions.

To maintain the analogy with EELs, the first layer of the top or bottom mirror in Fig. 2, as seen from the inner cavity, has to have a lower refractive index than the neighboring carrier confinement layer. The requirement of an alternating index sequence then leads to an integer number of Bragg pairs for the top mirror of an AlGaAs-based VCSEL, whereas a single low index quarter wave layer adjacent to the high index GaAs substrate has to be added to the bottom mirror. Here we assume that the top mirror is terminated by a low index material such as air.

Referring to index sequences $\bar{n}_\mathrm{c}|(\bar{n}_1|\,\bar{n}_2)^{M_\mathrm{Bt}}|\,\bar{n}_\mathrm{s}$ or $\bar{n}_\mathrm{c}|(\bar{n}_1|\,\bar{n}_2)^{M_\mathrm{Bb}}|\,\bar{n}_1|\,\bar{n}_\mathrm{s}$ for the Bragg reflectors and assuming a wave that is incident from a cladding material with index $\bar{n}_\mathrm{c}$ and is transmitted into a substrate of index $\bar{n}_\mathrm{s}$, the peak reflectivity of a top or bottom mirror with M_Bt or M_Bb layer pairs is found at the Bragg wavelength λ_B and is written as [20]

$$R_\mathrm{t,b} = \left(\frac{1 - b_\mathrm{t,b}}{1 + b_\mathrm{t,b}}\right)^2 \tag{6}$$

with

$$b_\mathrm{t} = \frac{\bar{n}_\mathrm{s}}{\bar{n}_\mathrm{c}}\left(\frac{\bar{n}_1}{\bar{n}_2}\right)^{2M_\mathrm{Bt}} \qquad \text{and} \qquad b_\mathrm{b} = \frac{\bar{n}_1^2}{\bar{n}_\mathrm{c}\bar{n}_\mathrm{s}}\left(\frac{\bar{n}_1}{\bar{n}_2}\right)^{2M_\mathrm{Bb}} \;, \tag{7}$$

where $\bar{n}_1 < \bar{n}_2$. Layer thicknesses $d_{1,2}$ have to be chosen as $d_{1,2} = \lambda_\mathrm{B}/(4\bar{n}_{1,2})$.

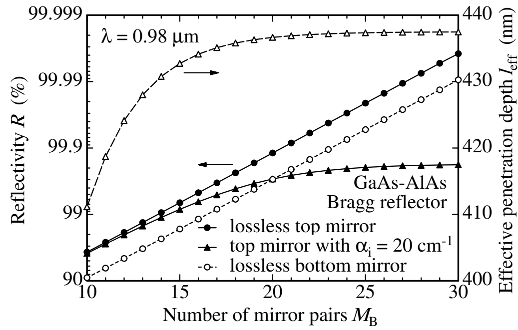

Fig. 3. Peak reflectivities of 980 nm GaAs-AlAs Bragg reflectors versus the number of mirror pairs. Data for the absorptive top mirror are calculated analytically from (13). The right-hand ordinate shows the effective penetration depth according to (9a) which is very similar for all three reflectors

Figure 3 shows top and bottom GaAs-AlAs Bragg mirror reflectivities as a function of the number of layer pairs calculated according to (6) and (7).

Waves are incident from $Al_{0.3}Ga_{0.7}As$ and are transmitted to air or GaAs in case of the top or bottom mirror, respectively, the latter having an additional AlAs quarter-wave layer. It can be seen that in case of a lossless top mirror, peak reflectivities exceeding 99.9 % are to be expected for more than 21 mirror pairs. Lower reflectivities of the bottom mirror arise from the smaller index contrast at the output interface.

Figure 4 displays the numerically determined spectral reflectivity $R(\lambda)$ and phase $\varphi_r(\lambda)$ for a Bragg mirror from Fig. 3. A broad spectral plateau of high reflectivity, often denoted as stop-band, appears around the Bragg wavelength λ_B, the width of which can be roughly estimated from [21], [2]

$$\Delta\lambda_{\text{stop}} \approx \frac{2\lambda_B \Delta\bar{n}_B}{\pi\langle\bar{n}_{\text{gr}}\rangle} \,. \tag{8}$$

The stop-band width is proportional to the refractive index step $\Delta\bar{n}_B = |\bar{n}_1 - \bar{n}_2|$, yielding $\Delta\lambda_{\text{stop}} \approx 100\,\text{nm}$ for the GaAs-AlAs composition from Fig. 3 with $\Delta\bar{n}_B = 0.56$ [22] and $\langle\bar{n}_{\text{gr}}\rangle \approx 3.6$ for the spatial average of the group index $\bar{n}_{\text{gr}} = \bar{n} - \lambda\, d\bar{n}/d\lambda$ at $\lambda_B = 980\,\text{nm}$. It has to be noted that only lossless mirrors or those with homogeneous absorption provide identical reflectivity spectra for waves being incident from the top or bottom side.

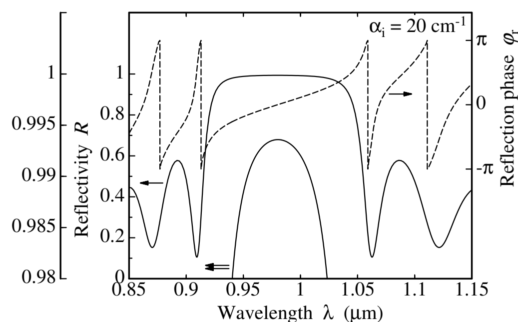

Fig. 4. Spectral dependence of the intensity reflection coefficient R and the phase φ_r of the amplitude reflection coefficient for the lossy top Bragg mirror from Fig. 3 with $M_{\text{Bt}} = 16$. The outer left-hand ordinate presents details of $R(\lambda)$ in the center of the stop-band, revealing substantial curvature of $R(\lambda)$

For incidence from a high index material, the phase φ_r of the complex amplitude reflection coefficient $r = \sqrt{R}\exp\{i\varphi_r\}$ is zero at the Bragg wavelength but varies almost linearly with phase coefficient β or inverse wavelength deviation, so that an effective mirror length l_{eff} can be defined, considering the phase penetration depth of the incident wave into the Bragg reflector. From the phase change, the penetration depth is obtained as

$$l_{\text{eff}} = -\frac{1}{2}\frac{\mathrm{d}\varphi_r}{\mathrm{d}\beta} = \frac{\lambda^2}{4\pi\langle\bar{n}_{\text{gr}}\rangle}\frac{\mathrm{d}\varphi_r}{\mathrm{d}\lambda} \approx \frac{\tanh(\kappa L_B)}{2\kappa} \tag{9a}$$

$$= \frac{\sqrt{R}}{2\kappa} = \frac{\sqrt{R}\lambda_B}{4\Delta\bar{n}_B} \approx \frac{\lambda_B}{4\Delta\bar{n}_B} \,, \tag{9b}$$

where the coupled-mode theory [2] is applied to obtain the first approximation, which can be further simplified to the last result in case of high reflectivities $\sqrt{R} \approx 1$. The coupling length equals $L_B = M_B(d_1 + d_2)$ and the coupling coefficient is $\kappa = 2\Delta\bar{n}_B/\lambda_B$ for a simple quarter-wave stack. The slow variation of l_{eff} with the number of mirror pairs M_B according to (9a) is plotted in Fig. 3, leading to $l_{\text{eff}} \approx 0.44\,\mu$m for the binary mirror under consideration. It should be noted that a more rigorous treatment of Bragg mirror properties distinguishes between phase and energy penetration depths [23], which, however, turn out to be very similar for usual semiconductor mirrors with small index steps. The total effective cavity length is finally determined as

$$L_{\text{eff}} = L + l_{\text{eff,t}} + l_{\text{eff,b}} \tag{10}$$

und can be used to estimate the longitudinal mode spacing from

$$\Delta\lambda_m \approx \frac{\lambda^2}{2L_{\text{eff}}\langle\bar{n}_{\text{gr}}\rangle} . \tag{11}$$

With $L_{\text{eff}} \approx 1.3\,\mu$m we get $\Delta\lambda_m \approx 110\,$nm, extending far beyond the mirror stop-band and even being larger than the spectral gain bandwidth of the QW material. Therefore just a single longitudinal mode can oscillate in a VCSEL with a thin inner cavity. The spectral position of this mode can readily be theoretically or experimentally determined by localizing the sharp dip appearing in the reflectivity spectrum of the complete layer stack. Note, however, that depending on the lateral size of the VCSEL several transverse modes may oscillate simultaneously, as discussed below.

2.3 Threshold Gain and Photon Lifetime

For lasing, the gain in the cavity has to balance the losses. With intrinsic losses α_i and α_a in the passive and active sections, respectively, considerations of gain enhancement and penetration of the waves into the Bragg reflectors lead to the lasing threshold condition

$$g_{\text{th}} = \alpha_a + \frac{1}{\Gamma_r d_a}\left[\alpha_i(L_{\text{eff}} - d_a) + \ln\frac{1}{\sqrt{R_t R_b}}\right] . \tag{12}$$

In general, α_i is a spatial average over the locally varying absorption coefficient, where weighting with the standing-wave intensity profile has to be applied. In this case, however, it is more convenient to determine the threshold gain g_{th} with the transfer matrix method. The intensity reflection coefficients R_t and R_b are valid for lossless top and bottom mirrors, respectively, and can, in the most simple cases, be determined from (6). Alternatively, the threshold condition can be formulated using the maximum reflectivity

$$R_\alpha \approx R\,\exp\{-2\alpha_i l_{\text{eff}}\} \approx R\,(1 - 2\alpha_i l_{\text{eff}}) \tag{13}$$

of a Bragg mirror with small losses $2\alpha_\mathrm{i} l_\mathrm{eff} \ll 1$, assuming that the wave traverses the distance l_eff back and forth. From (13) and the example in Fig. 3 it is seen that absorption imposes an upper limit on the achievable reflectivity of Bragg mirrors. Using (10), the threshold condition (12) is now rewritten as

$$g_\mathrm{th} = \alpha_\mathrm{a} + \frac{1}{\Gamma_\mathrm{r} d_\mathrm{a}} \left[\alpha_\mathrm{i}(L - d_\mathrm{a}) + \ln \frac{1}{\sqrt{R_{\mathrm{t}\alpha} R_{\mathrm{b}\alpha}}} \right] , \tag{14}$$

where the effective length L_eff is replaced by the inner cavity length L. Having determined the threshold gain, the photon lifetime τ_p is expressed as

$$\begin{aligned} \frac{1}{\tau_\mathrm{p}} = \frac{d_\mathrm{a}}{L_\mathrm{eff}} \langle v_\mathrm{gr} \rangle \Gamma_\mathrm{r} g_\mathrm{th} &\approx \langle v_\mathrm{gr} \rangle \left[\alpha_\mathrm{i} + \frac{1}{L_\mathrm{eff}} \ln \frac{1}{\sqrt{R_\mathrm{t} R_\mathrm{b}}} \right] \\ &\approx \langle v_\mathrm{gr} \rangle \left[\alpha_\mathrm{i} \frac{L}{L_\mathrm{eff}} + \frac{1}{L_\mathrm{eff}} \ln \frac{1}{\sqrt{R_{\mathrm{t}\alpha} R_{\mathrm{b}\alpha}}} \right] , \end{aligned} \tag{15}$$

with the first approximation holding for the usually satisfied conditions $\alpha_\mathrm{a} \ll g_\mathrm{th}$ and $d_\mathrm{a} \ll L_\mathrm{eff}$. The average group velocity is related to the vacuum velocity of light c as $\langle v_\mathrm{gr} \rangle = c / \langle \bar{n}_\mathrm{gr} \rangle$. With $\langle \bar{n}_\mathrm{gr} \rangle = 3.6$, $L_\mathrm{eff} = 1.3\,\mu\mathrm{m}$, $R_\mathrm{t} = R_\mathrm{b} = 99.5\,\%$ and $\alpha_\mathrm{i} = 10\,\mathrm{cm}^{-1}$ we obtain $\tau_\mathrm{p} = 2.5\,\mathrm{ps}$ and $g_\mathrm{th} = 1460\,\mathrm{cm}^{-1}$ for $d_\mathrm{a} = 24\,\mathrm{nm}$ and $\Gamma_\mathrm{r} = 1.8$.

2.4 Matrix Method and Standing-Wave Pattern

For the design of high performance VCSELs it is important to know the electric field distribution in the resonator. Assuming linearly polarized waves in a one-dimensional scalar approach, we have to solve the Helmholtz equation

$$\frac{\mathrm{d}^2 E(z)}{\mathrm{d}z^2} + \gamma^2 E(z) = 0 \tag{16}$$

for the phasor of the transverse electric field component $E = E_x$ in the multilayer system depicted in Fig. 5. The complex propagation coefficient

$$\gamma_m = \beta_m - \mathrm{i}\alpha_m / 2 \tag{17}$$

with the imaginary unit $\mathrm{i} = \sqrt{-1}$ is constant in each homogeneous layer of index m, and the absorption coefficient fulfills $\alpha_m \geq 0$ except from the QW layers, where gain leads to $\alpha_m < 0$. The real part β_m of the propagation coefficient is related to the refractive index $\bar{n}_m$ by

$$\beta_m = 2\pi \bar{n}_m / \lambda \, . \tag{18}$$

In each layer, the electric field is the superposition

$$E_m(z) = E_m^+ \exp\{-\mathrm{i}\gamma_m (z - z_m)\} + E_m^- \exp\{+\mathrm{i}\gamma_m (z - z_m)\} \tag{19}$$

of two monochromatic plane waves of $\exp\{\mathrm{i}\omega t\}$ harmonic time dependence, counterpropagating in z-direction. According to Fig. 5, E_m^+ and E_m^- denote

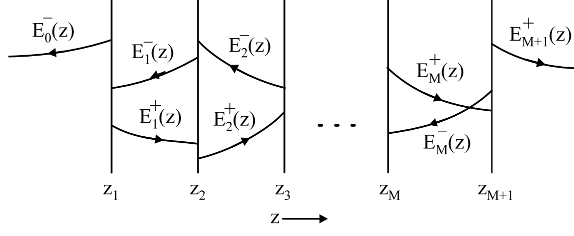

Fig. 5. Multilayer structure and traveling wave components for the one-dimensional transfer matrix method

the complex field amplitudes of the waves at the interface $z = z_m$ in section m with $z_m \le z \le z_{m+1}$, where $m = 1, \ldots, M$ with M as the total number of layers.

The continuity conditions for the transverse components of electric and magnetic fields lead to relations

$$\begin{aligned} E_m^+ &= (\gamma_m^+ E_{m+1}^+ + \gamma_m^- E_{m+1}^-) \exp\{i\gamma_m (z_{m+1} - z_m)\} , \\ E_m^- &= (\gamma_m^- E_{m+1}^+ + \gamma_m^+ E_{m+1}^-) \exp\{-i\gamma_m (z_{m+1} - z_m)\} \end{aligned} \tag{20}$$

between amplitudes in subsequent layers, where abbreviations

$$\gamma_m^+ = \frac{\gamma_m + \gamma_{m+1}}{2\gamma_m} \qquad \text{and} \qquad \gamma_m^- = \frac{\gamma_m - \gamma_{m+1}}{2\gamma_m} \tag{21}$$

have been introduced. Relations (20) establish the well-known transfer matrix method [24] for calculating the electric field in a multilayer stack. Self-oscillation of the layer structure exclusively allows outgoing waves in the terminating sections $m = 0$ and $m = M + 1$, i.e.

$$E_0^+ = 0 \qquad \text{and} \qquad E_{M+1}^- = 0 . \tag{22}$$

These kinds of solutions are possible only for sufficiently large gain in the active layers. Conditions (20)–(22) thus simultaneously fix the lasing wavelength and threshold gain of all longitudinal modes [25].

Figure 6 shows the result of a numerical calculation of the electric field distribution for a model VCSEL that contains three active InGaAs QWs in the center, an 18 pairs GaAs-$Al_{0.7}Ga_{0.3}As$ top and a 24.5 pairs GaAs-AlAs bottom Bragg reflector. It is seen that, due to the high reflectivities of the mirrors, a pronounced resonant enhancement of the field amplitude is built up. In the given example, the half-width of the envelope is 1.7 µm, and the field amplitude in the antinode at the surface is less than 10 % of the maximum value found near the center. Details of the standing-wave pattern together with the conduction band edge profile in flat band approximation are already displayed in Fig. 2. In the Bragg reflectors, single-step grading of the heterointerfaces has been introduced to reduce the potential barrier and thus the electrical resistance. Grading is especially important at those heterojunctions that are electrically driven in backward direction, which, in the present design, just occur at nodes of the standing-wave pattern. It is thus

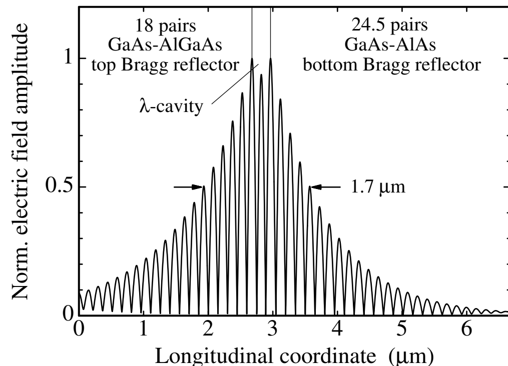

Fig. 6. Standing-wave pattern of the electric field in a VCSEL. Details of the λ-cavity region are displayed in Fig. 2

possible to apply modulation doping in the mirrors in order to optimize the current–voltage characteristics without significantly increasing the threshold gain [26]. It should be noted that several bandgap engineering techniques like multi-step, superlattice-type, or continuous gradings have been successfully applied in practice. Adverse effects on the mirror reflectivities can be kept small with thin intermediate layers or can be compensated for by increasing the mirror thickness. The AlAs layer in the top Bragg reflector in Fig. 2 serves to provide current and photon confinement after selective oxidation, which will be discussed in Sects. 3.1 and 3.4.

2.5 Energy Flux and Differential Quantum Efficiency

Above threshold current I_{th}, top and bottom light output powers P_{t} and P_{b} linearly increase with driving current I [1]–[3]. We write

$$P_{\mathrm{t,b}} = \tilde{\eta}_{\mathrm{dt,b}} \frac{\hbar\omega}{q} \left(I - I_{\mathrm{th}}\right) , \tag{23}$$

where we have defined the reduced differential quantum efficiency $\tilde{\eta}_{\mathrm{dt,b}}$ describing the fraction of injected electrons that produce coherent emission in the top or bottom external beam, and $\hbar\omega$, q denote photon energy and electron charge, respectively. In order to consider carrier overflow over confining barriers as well as lateral leakage currents, we introduce a current injection efficiency η_I and put

$$\tilde{\eta}_{\mathrm{dt,b}} = \eta_{\mathrm{dt,b}} \eta_I , \tag{24}$$

where the differential quantum efficiency $\eta_{\mathrm{dt,b}}$ characterizes the percentage of generated coherent light that is available as top or bottom emission. In well designed VCSELs with high quality active QWs, $\eta_I > 90\,\%$ can be achieved. Due to absorption in the mirrors we always[2] find $\eta_{\mathrm{dt}} + \eta_{\mathrm{db}} < 100\,\%$.

[2] Differential quantum efficiencies $\tilde{\eta}_{\mathrm{d}} = \tilde{\eta}_{\mathrm{dt}} + \tilde{\eta}_{\mathrm{db}} > 1$ can regularly be obtained in diode cascade structures at the expense of higher operating voltages [27], [28].

The emitted coherent power is related to the time averaged Poynting vector [2] $\boldsymbol{S} = \mathrm{Re}\{\boldsymbol{E} \times \boldsymbol{H}^*\}$ with $*$ denoting complex conjugation. In the one-dimensional scalar approach used in the preceeding section the (linearly polarized) magnetic field is

$$H = H_y = \frac{\mathrm{i}}{\omega\mu_0} \frac{\mathrm{d}E}{\mathrm{d}z} \;, \tag{25}$$

and energy flux occurs in $\pm z$-directions only. Using (19) and (25) yields for the energy flux in section m of the multilayer structure the expression

$$\begin{aligned} S_m(z) = {} & \frac{\beta_m}{\omega\mu_0} |E_m^+|^2 \exp\{-\alpha_m(z - z_m)\} - \frac{\beta_m}{\omega\mu_0} |E_m^-|^2 \exp\{\alpha_m(z - z_m)\} \\ & + \frac{\alpha_m}{\omega\mu_0} \mathrm{Im}\left\{E_m^+ (E_m^-)^* \exp\{-\mathrm{i}2\beta_m(z - z_m)\}\right\} \;. \end{aligned} \tag{26}$$

The first and second term describe the energy flux of the forward and backward propagating waves, respectively. The third term takes into account energy exchange that arises in media with gain or loss.

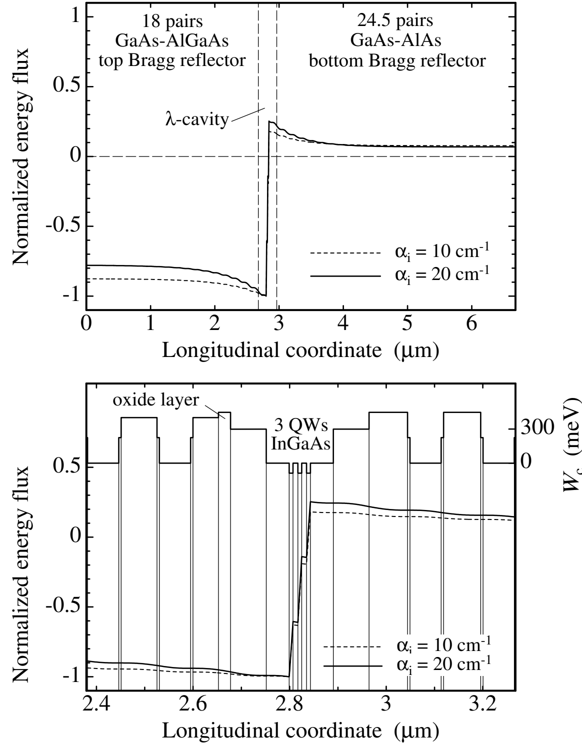

Fig. 7. Normalized energy flux density corresponding to the VCSEL electric field distributions of Figs. 6 **(top)** and 2 **(bottom)**

Figure 7 depicts the energy flux for the standing-wave patterns of Figs. 2 and 6. It becomes clear that power is generated in the QWs only. Extrema in the energy flux are found on both sides of the three QW system, and power flux occurs toward the Bragg reflectors ($S < 0$ signifies energy transport in $-z$-direction), where the flux is diminished due to absorption. The differential quantum efficiency for top and bottom emission $\eta_\mathrm{d} = \eta_\mathrm{dt} + \eta_\mathrm{db}$ is identified as the fraction of the generated flux that is emitted through top or bottom mirrors, i.e. [29]

$$\eta_\mathrm{d} = \frac{g_\mathrm{th}}{g_\mathrm{th} + \alpha_\mathrm{a}} \left(1 + \frac{\sum_{i,\mathrm{pass.}} \Delta S_i}{\sum_{i,\mathrm{act.}} \Delta S_i} \right) \quad \text{with} \quad \Delta S_i = S(z_{i+1}) - S(z_i) \;, \tag{27}$$

where g_th is the threshold gain previously determined by the transfer matrix method. The sum in the numerator or denominator extends over all passive or active segments, respectively. Obviously, absorption leads to flux increments $\Delta S_i < 0$ and thus to $\eta_\mathrm{d} < 1$. Denoting top and bottom emitted energy flux by $S_\mathrm{t} = S(z_1) < 0$ and $S_\mathrm{b} = S(z_{M+1}) > 0$, respectively, the corresponding differential quantum efficiencies are

$$\eta_\mathrm{dt} = \eta_\mathrm{d} \frac{|S_\mathrm{t}|}{|S_\mathrm{t}| + |S_\mathrm{b}|} \qquad \text{and} \qquad \eta_\mathrm{db} = \eta_\mathrm{d} \frac{|S_\mathrm{b}|}{|S_\mathrm{t}| + |S_\mathrm{b}|} \;. \tag{28}$$

Figures 2 and 6 have been calculated with constant $\alpha_\mathrm{i} = 20\,\mathrm{cm}^{-1}$. In general, spatially varying absorption can be accurately taken into account in the transfer matrix computation. To illustrate the effect of reduced average absorption on the energy flux distribution, as to be achieved by modulation doping, a curve with $\alpha_\mathrm{i} = 10\,\mathrm{cm}^{-1}$ has been included in Fig. 7. Compared to values $g_\mathrm{th} = 1820\,\mathrm{cm}^{-1}$ and $\eta_\mathrm{d} = 67\,\%$ before, threshold gain and differential efficiency are modified to $g_\mathrm{th} = 1520\,\mathrm{cm}^{-1}$ and $\eta_\mathrm{d} = 80\,\%$, respectively, such that $g_\mathrm{th} \cdot \eta_\mathrm{d} \approx const.$ Without any loss, horizontal lines $S(z)$ would appear in the passive layers in Fig. 7.

2.6 Conversion Efficiency

Wallplug or conversion efficiency η_c for emission through the top or bottom mirror is defined as the ratio of coherent light output power and electrical input power

$$\eta_\mathrm{ct,b} = \frac{P_\mathrm{t,b}}{IV} \;, \tag{29}$$

where V is the voltage applied across the VCSEL. In an ideal device one would expect a current–voltage characteristics of the form

$$V \approx V_\mathrm{k} + R_\mathrm{s} I \;, \tag{30}$$

where $R_\mathrm{s} = \mathrm{d}V/\,\mathrm{d}I$ denotes the differential series resistance, and the kink voltage V_k is related to the separation of quasi-Fermi energies but can be

approximated by $V_\mathrm{k} \approx \hbar\omega/q$. Non-perfect grading of heterointerfaces induces a larger voltage offset accompanied by a pronounced curvature of the I–V characteristics [30]. Using (23), (24), (29), and (30) leads to

$$\eta_\mathrm{ct,b} = \eta_\mathrm{dt,b}\eta_I \frac{\hbar\omega}{q} \frac{I - I_\mathrm{th}}{IV_\mathrm{k} + I^2 R_\mathrm{s}} , \tag{31}$$

showing that for $I \gg I_\mathrm{th}$ the series resistance is responsible for the decrease of $\eta_\mathrm{ct,b}$ with increasing current. Efficiency is maximized at the laser current

$$\hat{I}_\mathrm{c} = I_\mathrm{th} \cdot \left(1 + \sqrt{1+\xi}\right) \qquad \text{with} \qquad \xi = \frac{V_\mathrm{k}}{I_\mathrm{th} R_\mathrm{s}} , \tag{32}$$

from which the peak conversion efficiency is obtained as

$$\hat{\eta}_\mathrm{ct,b} = \eta_\mathrm{dt,b}\eta_I \frac{\hbar\omega}{qV_\mathrm{k}} \frac{\xi}{(1+\sqrt{1+\xi})^2} = \eta_\mathrm{dt,b}\eta_I \frac{\hbar\omega}{qV_\mathrm{k}} f_\mathrm{c}(\xi) . \tag{33}$$

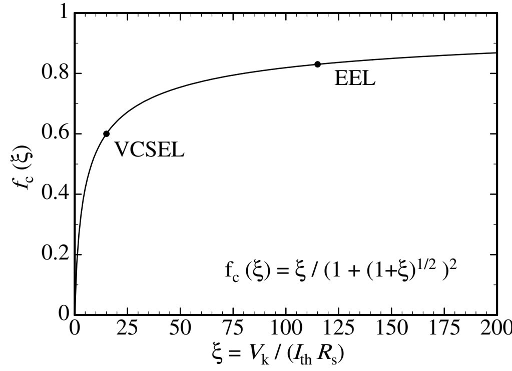

Fig. 8. Electrical to optical conversion function for laser diodes with linear current–voltage characteristics. Data for the VCSEL and the EEL are taken from [12] and [31], respectively

Figure 8 shows the conversion function $f_\mathrm{c}(\xi)$, approaching $f_\mathrm{c}(\xi) \to 1$ only slowly with increasing ξ. Even for perfect injection and differential quantum efficiencies as well as a kink voltage close to the photon energy equivalent voltage $\hbar\omega/q$, maximum obtainable efficiencies cannot exceed f_c. For high efficiency lasers it is certainly desired to strive for small products $I_\mathrm{th}R_\mathrm{s}$ or equivalently $j_\mathrm{th}\bar{R}_\mathrm{s}$ with threshold current density $j_\mathrm{th} = I_\mathrm{th}/A_\mathrm{a}$, sheet resistance $\bar{R}_\mathrm{s} = R_\mathrm{s}A_\mathrm{a}$, and active area A_a. Unfortunately for VCSELs, the usually thick multilayer stack leads to higher sheet resistances compared to EELs[3]. Likewise, thin QW gain regions with small roundtrip gain induce higher threshold current densities. For these reasons, VCSEL conversion efficiency curves, as displayed below, show rollover at currents much closer to

[3] Although small area VCSELs appear to have fairly competitive sheet resistances, threshold current densities tend to be in the $\mathrm{kA/cm^2}$ range.

threshold current compared to, e.g., broad-area EELs for high-power applications. Figure 8 contains data points for a record EEL [31] and an optimized VCSEL [12] with conversion efficiency rollover close to $5 \cdot I_{\mathrm{th}}$. Since there exists a usual tradeoff between increasing layer conductivity or decreasing threshold gain while maintaining high differential efficiencies, it becomes clear that obtaining peak conversion efficiencies above 60 % is one of the most challenging topics in VCSEL research. On the other hand, due to low threshold currents, VCSELs readily offer fairly high η_{c} at low output powers even in the sub-mW range, which is of special importance for parallel optical interconnect applications and not at all easily achieved with EELs.

3 Emission Characteristics of Oxide-Confined VCSELs

The following section will concentrate on experimental emission data of selectively oxidized VCSELs. We first describe VCSEL layout and fabrication, show operation behavior of multi as well as single transverse mode devices and arrays and look into the origins of observed temperature characteristics. Transverse modes are introduced in a general Laguerre–Gaussian approximative manner and effective index guiding in oxidized VCSELs is finally explained.

3.1 Device Structure

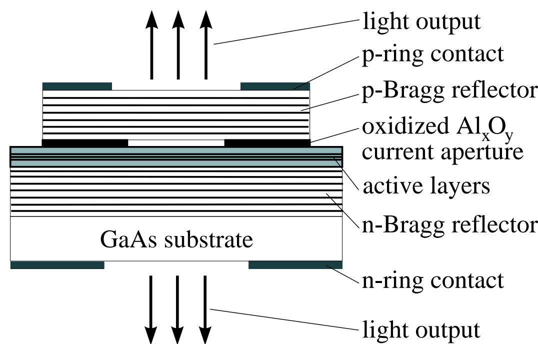

Fig. 9. Schematics of a selectively oxidized VCSEL

Figure 9 illustrates the general configuration of selectively oxidized VCSELs investigated. The multilayer system is grown by solid source molecular beam epitaxy on *n*-GaAs substrate. For emission wavelengths in the 980 nm (850 nm) spectral region, the active layer consists of half-wavelength thick GaAs ($Al_{0.2}Ga_{0.8}As$) with three, each 8 nm thick compressively strained $In_{0.2}Ga_{0.8}As$ (unstrained GaAs) QWs separated by 10 nm barriers in the center. Quarter-wavelength $Al_{0.4}Ga_{0.6}As$ ($Al_{0.5}Ga_{0.5}As$) cladding layers are

introduced on both sides of the active region to improve longitudinal carrier confinement and to make the inner region one wavelength thick. Top and bottom mirrors contain $Al_{0.7}Ga_{0.3}As$-GaAs ($Al_{0.9}Ga_{0.1}As$-$Al_{0.2}Ga_{0.8}As$) quarter-wavelength Bragg stacks. Single-step grading with 5 nm thick layers of intermediate bandgap energy is used to reduce the electrical series resistance. Current is supplied through the carbon *p*-doped top and silicon *n*-doped bottom reflectors, where modulation and δ-doping is required for high performance devices [30]. Current confinement is achieved by means of selective lateral oxidation [8] of an about 30 nm thick extra AlAs layer placed directly above the top cladding layer (see Fig. 2). Oxidation is done in a 400 °C hot water vapor atmosphere [12], leading to lateral oxidation rates in the 1 µm/min. range, and requires wet or dry mesa etching. Applying TiPtAu top and AuGeNi bottom ring contacts, simultaneous top and bottom laser emission from InGaAs QWs is obtained. The etched mesa size might be chosen several 10 µm larger than the envisaged active diameter which can be adjusted from, e.g., 1 µm to above 100 µm by proper choice of mesa size and oxidation time.

3.2 Experimental Operating Characteristics

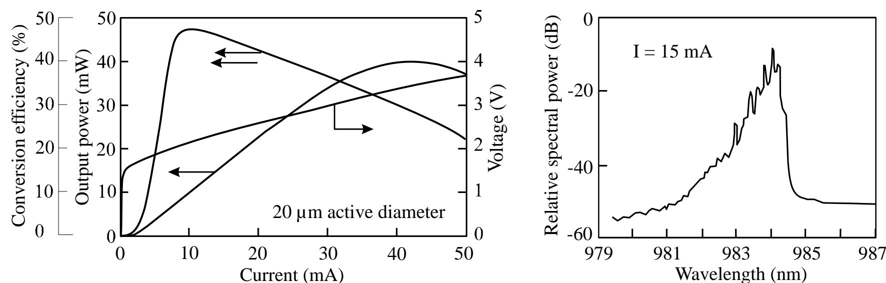

Fig. 10. Output power, conversion efficiency, and current–voltage characteristics of a high efficiency selectively oxidized InGaAs QW VCSEL of 20 µm diameter **(left)** and emission spectrum at $I = 15$ mA driving current **(right)**

Figure 10 shows output characteristics of a 20 µm active diameter InGaAs QW highly efficient oxidized VCSEL [32]. Threshold current and threshold voltage are 3 mA and 1.65 V, respectively. Due to the differential resistance of less than 40 Ω under lasing conditions, driving voltage remains below 3.5 V up to the maximum output power of 40 mW which is limited by thermal rollover in the non heat-sinked device. Maximum conversion efficiency of $\hat{\eta}_{\mathrm{ct}} = 47\,\%$ is observed for a driving current of 10 mA at an output power of 10 mW, where several transverse modes oscillate simultaneously. The mode spacing is about 0.2 nm and the total −10 dB spectral emission bandwidth is less than 2 nm. The emission spectrum changes rapidly with increasing bias current and

higher order, shorter wavelength modes become more dominant. The high wallplug efficiency is related to the favorable top side differential quantum efficiency of $\tilde{\eta}_{\mathrm{dt}} \approx 90\,\%$. Owing to the comparatively large driving voltage at optimum power conversion, the electrical series resistance consumes about 40 % of the total input power. Other sources of losses are bottom emission, carrier escape, and internal absorption and scattering in the mirrors as well as the active region. From an estimate of the various contributions it is clear that the injection efficiency fulfills $\eta_I > 90\,\%$, which is also in accordance with the differential quantum efficiency measured. Record power conversion efficiencies reported to date rise above 50 % [11], [12] and are obtained from multimode devices in the 5 to 12 μm active diameter range.

Top-emitting VCSELs of larger active sizes begin to suffer from laterally inhomogeneous current supply due to current crowding at the oxide aperture edge and tend to develop ring-shaped near- and far-field patterns. Homogeneous large-area emission can be achieved from bottom-emitting devices with appropriate heat-sinking [33].

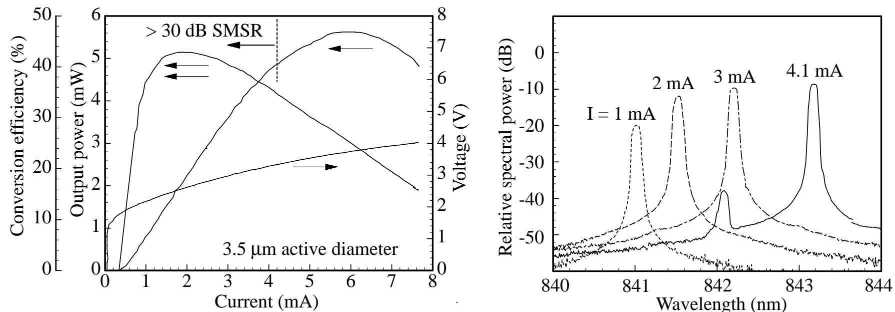

Fig. 11. Operation characteristics **(left)** and current dependent emission spectra **(right)** of a 3.5 μm active diameter GaAs QW singlemode VCSEL

In contrast to transverse multimode devices, Fig. 11 illustrates the operation behavior of a small diameter oxide-confined VCSEL exhibiting high singlemode output powers [34]. The GaAs QW device is designed for emission in the 850 nm spectral region, being defined as a standard for short-distance optical interconnects. Threshold current is about 500 μA and the maximum fundamental mode output power of 4.8 mW is achieved at a driving current of 4.1 mA, corresponding to a wallplug efficiency of 35 %. The singlemode emission limit is defined through a side-mode suppression ratio (SMSR) of larger than 30 dB. Maximum power conversion of $\hat{\eta}_{\mathrm{ct}} = 42\,\%$ occurs at $I = 2\,\mathrm{mA}$ and $P_{\mathrm{t}} = 2.2\,\mathrm{mW}$. The red-shift of the emission spectra with increasing current indicates internal heating of the VCSEL, which is discussed in Sect. 3.3. The onset of the higher azimuthal order, donut-shaped transverse mode for high currents is initiated by fundamental mode spatial hole burning and

thermally induced waveguiding. It should be mentioned that VCSELs with much smaller threshold currents in the sub-100 µA range have already been demonstrated [13], choosing small active diameters and high mirror reflectivities, however, greatly restricting achievable output power levels.

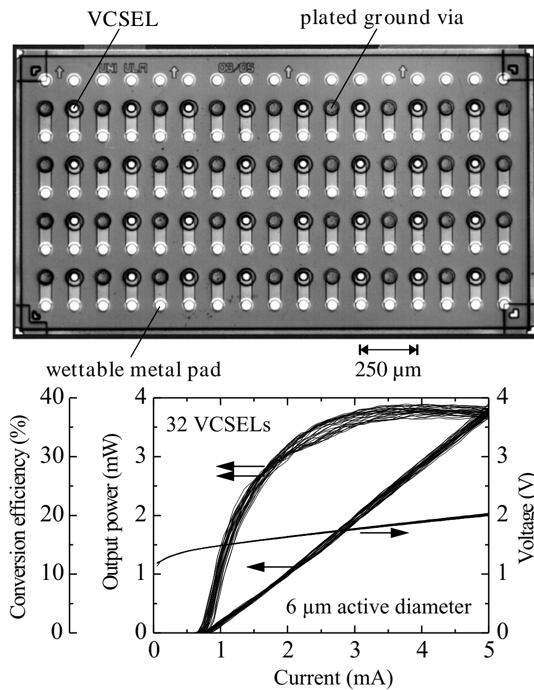

Fig. 12. Layout **(top)** and static operation characteristics **(bottom)** of a 4×8 element, 6 µm individual device diameter bottom-emitting VCSEL array suitable for flip-chip mounting

Due to their surface-normal emission, VCSELs especially lend themselves to form one- and two-dimensional arrays [35]–[41] for various applications including highly parallel optical interconnects. Figure 12 presents layout and characteristics of a VCSEL array consisting of 32 individually addressable devices arranged in a 4×8 matrix, designed for hybrid integration by direct flip-chip bonding onto Si CMOS circuits [42], [43]. The particular array shows transverse multimode emission at 990 nm wavelength with excellent homogeneity of L–I and I–V curves. The device pitch of 250 µm is well suited for direct coupling into dense arrays of silica or plastic optical fibers to establish inter- and intra-cabinet data links down to optical backplanes in advanced computer environments that require channel data rates in the several Gbit/s regime.

3.3 Temperature Behavior

Due to the short optical resonator, the emission wavelength λ of a VCSEL is determined by the cavity resonance and not by the gain peak as in conventional Fabry-Pérot type EELs. The thermal wavelength shift is thus mainly governed by changes of the average refractive index in the resonator and to a lesser extent (about 10 %) by the thermal expansion of the semiconductor layers. Consequently, the wavelength shift of the mode depends on the material composition of the Bragg reflectors and the inner cavity. For VCSELs in the 800 to 1000 nm emission wavelength range the mode shift is typically found to be $\partial\lambda/\partial T \approx 0.07\,\mathrm{nm/K}$. With this ratio, internal temperature rises can be estimated from measured spectra as in Fig. 11.

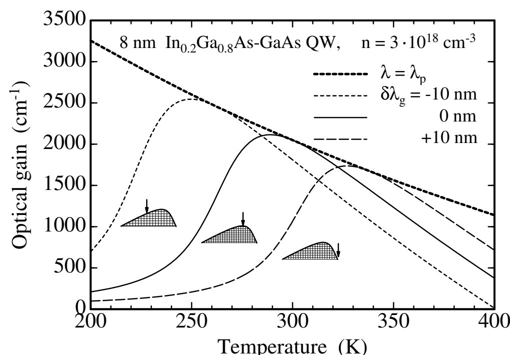

Fig. 13. Modal material gain coefficient as a function of temperature. Upper dashed curve for $\lambda = \lambda_\mathrm{p}$ is the peak gain. Lower curves are calculated for different gain offsets $\delta\lambda_\mathrm{g}$ at room temperature. Modal positions at $T = 300\,\mathrm{K}$ are indicated as arrows in the cross hatched spectral gain profiles in the insets

On the other hand, the active QWs show a shift of the peak material gain wavelength λ_p according to $\partial\lambda_\mathrm{p}/\partial T \approx 0.32\,\mathrm{nm/K}$ basically due to bandgap shrinkage. Because of differing gain and mode shifts with increasing current and thus device temperature, a mutual shift of lasing mode and gain spectrum occurs. Figure 13 illustrates the resulting material gain experienced by the VCSEL mode as a function of temperature T. Calculations are performed for an 8 nm thick $\mathrm{In_{0.2}Ga_{0.8}As}$-GaAs QW at a fixed carrier density of $n = 3 \cdot 10^{18}\,\mathrm{cm}^{-3}$. Although the peak gain continuously decreases with increasing temperature, the gain seen by the mode can decrease or increase depending on the amount of wavelength detuning at room temperature, which is characterized in Fig. 13 by the offset $\delta\lambda_\mathrm{g} = \lambda(T = 300\,\mathrm{K}) - \lambda_\mathrm{p}(\mathrm{T} = 300\,\mathrm{K})$. The offset $\delta\lambda_\mathrm{g}$ can be adjusted during epitaxial growth of the VCSEL structure. Of great practical interest is the choice $\delta\lambda_\mathrm{g} > 0$. Starting from operation at room temperature, with increasing laser current or ambient temperature the gain available for the mode increases, thus compensating for the decay of the peak gain and temperature dependent loss mechanisms in the active layer. In this way, a rather temperature insensitive behavior of the VCSEL output characteristics can be obtained.

In connection with Fig. 13 it should be noted that the maximum modal material gain and thus the minimum VCSEL threshold current is not obtained for optimum alignment of mode and gain peak but is found at lower temperatures with a negative detuning. Whereas this effect is relatively small in high quality InGaAs or GaAs QW active material, it has to be taken into account for the design of long-wavelength VCSELs based on InP [44].

Heating of the VCSEL is suitably described by the thermal resistance

$$R_{\mathrm{th}} = \frac{\Delta T}{P_{\mathrm{diss}}} \, , \tag{34}$$

defined by the ratio of temperature increase ΔT in the device and dissipated electrical power P_{diss}. For VCSELs with high wallplug efficiency it is important to use

$$P_{\mathrm{diss}} = IV - P_{\mathrm{t}} - P_{\mathrm{b}} = IV - P = IV(1 - \eta_{\mathrm{c}}) \tag{35}$$

instead of the electrical input power since otherwise one would neglect photon cooling by the radiated optical power P. The thermal resistance obeys the simple relation [45]

$$R_{\mathrm{th}} \approx \frac{1}{2\lambda_{\mathrm{c}} D_{\mathrm{a}}} \, , \tag{36}$$

which is obtained assuming heat flow from a circular area with diameter D_{a}, identified here as the active diameter, into a half-space filled with a medium of thermal conductivity λ_{c}. Thermal resistances plotted in Fig. 14 were measured for substrate-down mounted top- as well as bottom-emitting devices. The thermal resistance is determined experimentally as $R_{\mathrm{th}} = C_1/C_2$ from two measurements, namely the wavelength shift with consumed power, $C_1 = \Delta\lambda/\Delta P_{\mathrm{diss}}$, and the shift with varying heat-sink temperature, $C_2 = \Delta\lambda/\Delta T_{\mathrm{hs}}$, usually at pulsed operation, i.e. at negligible dissipated power. As mentioned before, $C_2 \approx 0.07\,\mathrm{nm/K}$ for short-wavelength VCSELs. The solid lines are curve fits according to (36), leading to average thermal conductivities of the multilayer stack close to that of the GaAs substrate. Thermal resistances of VCSELs can be considerably reduced by upside-down mounting on a heat-spreader, requiring, however, bottom emission through a transparent substrate or even substrate removal.

With increasing driving current above threshold or increasing ambient temperature a typical rollover of the output power characteristics is observed. Higher carrier densities to maintain the threshold gain, carrier and current leakage effects, as well as increased nonradiative recombinations are generally made responsible for the deviation from the linear increase of output power with current. Figure 15 shows output characteristics of an oxidized VCSEL for various heat-sink temperatures up to $T_{\mathrm{hs}} = 185\,^\circ\mathrm{C}$. By observing the red-shift of the emission spectrum, it is found [12] that for room temperature operation, rollover occurs at about $\Delta T = 90\,\mathrm{K}$ intrinsic temperature rise,

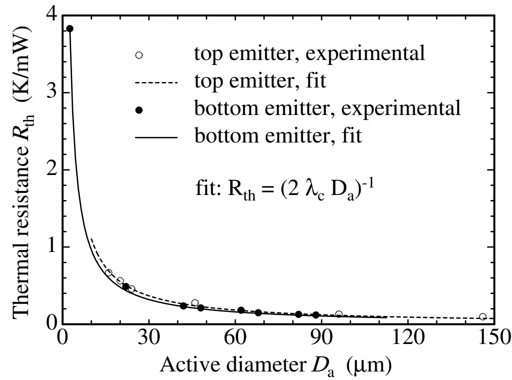

Fig. 14. Experimental and fitted thermal resistances of substrate side mounted top- and bottom-emitting VCSELs as a function of active diameter D_a

whereas laser turn-off at $T \approx 200\,°C$ is fairly independent of T_{hs}. More detailed analysis of the output characteristics in Fig. 15 shows that in a reduced temperature interval between −40 to +80 °C that is of primary technical interest for datacom applications, the threshold current varies between 300 and 500 µA, while the laser current required for 1 mW output power ranges between 1.5 and 1.85 mA. The results clearly demonstrate that well designed VCSELs can operate over an extremely wide temperature range, often even making external temperature control unnecessary.

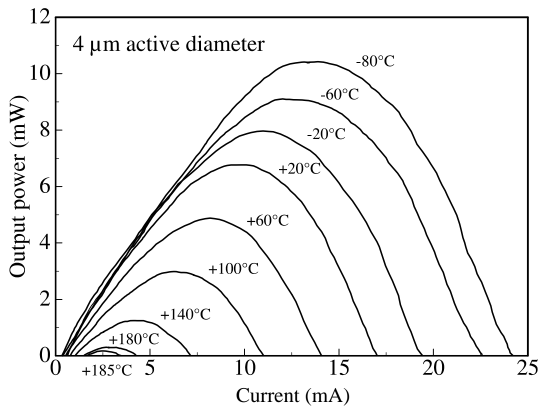

Fig. 15. Continuous-wave operation light-current curves of a VCSEL with 4 µm active diameter for various heat-sink temperatures from −80 to +185 °C [12] (© 1997 IEEE)

3.4 Transverse Modes

Analyzing the transverse mode behavior of VCSELs is a rather complex subject. The number and intensity of oscillating modes is related to the balance between optical losses during round-trip propagation in the cavity and amplification in the short active section of the device. Losses are due to absorption,

scattering, as well as diffraction and largely depend on the vertical waveguiding properties of the multilayer stack. Unfortunately, in the most promising device designs to date, waveguide-like structures cannot be easily identified and are even inhomogeneous in the propagation direction. In the active layers, amplification is non-uniform among different modes owing to varying spatial overlaps between optical gain and mode intensity profiles. Rather unimpressed by the amount of complexity involved, modes emitted from circularly symmetric VCSEL structures prefer to closely resemble the profiles of the Laguerre–Gaussian mode family [46], constituting the eigenfunctions for guided wave propagation in a quadratic refractive index medium. In planar proton-implanted VCSELs, a correspondence to this refractive index distribution can be found in the thermally induced index profile that is established as a result of internal heating [29], and even the more step-like effective index profile in selectively oxidized VCSELs dicussed below can be roughly approximated in this way.

The near-field intensity profiles of the modes are written as

$$\begin{aligned} S_{lp}(r,\varphi) &\propto |E_{lp}(r,\varphi)|^2 \\ &\propto \left(\frac{2r^2}{w_0^2}\right)^l \left[L_{p-1}^{(l)}\left(\frac{2r^2}{w_0^2}\right)\right]^2 \begin{Bmatrix} \cos^2(l\varphi) \\ \sin^2(l\varphi) \end{Bmatrix} \exp\left\{-\frac{2r^2}{w_0^2}\right\} \end{aligned} \tag{37}$$

where (r,φ) are cylindrical coordinates and $L_{p-1}^{(l)}$ is the generalized Laguerre polynomial of kind l and order $p-1$, with integers l and p characterizing the azimuthal and radial mode orders, respectively. Nomenclature of mode orders is chosen in analogy to linearly polarized LP_{lp} optical fiber modes. From (37), the fundamental mode

$$S_{01}(r) \propto \exp\left\{-\frac{2r^2}{w_0^2}\right\} \tag{38}$$

is of simple Gaussian shape with azimuthal symmetry. All modes still can oscillate in two different states of polarization. Including polarization, the degeneracy of modes with $l \geq 1$ is fourfold, whereas it is twofold for $l = 0$. The mode field radius or spot radius w_0 is expressed as

$$w_0 = \sqrt{\frac{a\lambda}{\pi\sqrt{\bar{n}_0^2 - \bar{n}_\mathrm{a}^2}}}\ , \tag{39}$$

introducing the distance a at which the refractive index profile

$$\bar{n}^2(r) = \bar{n}_0^2 - (\bar{n}_0^2 - \bar{n}_\mathrm{a}^2) \cdot (r/a)^2 \tag{40}$$

has dropped from $\bar{n}(r = 0) = \bar{n}_0$ at the waveguide center to the value $\bar{n}(r = a) = \bar{n}_\mathrm{a}$. Near-field mode profiles according to (37) can be easily transformed into the far-field and thus be conveniently accessed experimentally. In particular for the fundamental mode, the full far-field angle at which the intensity has dropped to one-half of its maximum writes as

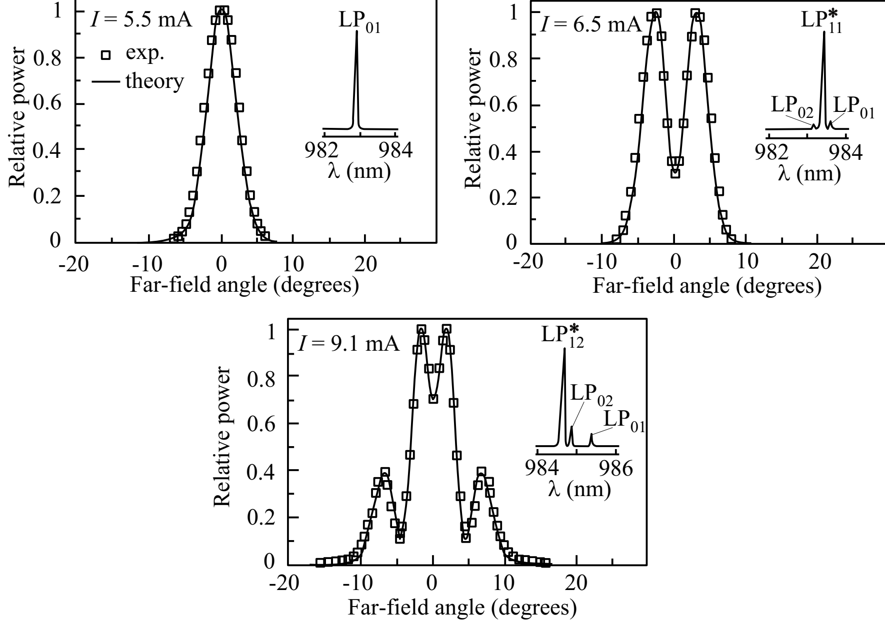

Fig. 16. Measured and calculated far-field distributions of a 19 μm diameter proton-implanted VCSEL as well as corresponding emission spectra for different driving currents above threshold current $I_{\mathrm{th}} = 4.9\,\mathrm{mA}$ [47] (© 1995 IEEE)

$\Theta_{\mathrm{FWHM}} \approx \sqrt{2\ln 2}\,\lambda/(\pi w_0)$, where the approximation holds for angles satisfying $\tan\Theta \approx \Theta$.

As an example, Fig. 16 shows measured and calculated far-field distributions of a large diameter planar proton-implanted VCSEL [47]. For the calculation, spot diameters (39) are determined self-consistently by taking the generated internal temperature profile into account. Far-fields are then obtained from a superposition of different mode intensities, the weighting of which is taken from the experimental emission spectra. In the insets in Fig. 16, the asterisks at the LP_{11} and LP_{12} modes indicate superposition of the $\cos^2(l\varphi)$ and $\sin^2(l\varphi)$ terms in (37) to obtain the experimentally observed azimuthally symmetric mode profiles. Increasing the current leads to a red-shift of the overall spectrum due to pronounced heating. Stronger waveguiding and photon-carrier interactions like spatial hole burning favor oscillation of shorter-wavelength modes of increasingly higher order. In general, the Gaussian fundamental mode is followed by the LP_{11} donut mode with vanishing on-axis intensity. It is seen that an excellent correspondence between measurement and calculation is obtained, supporting the applicability of the simplified Laguerre–Gaussian field approach. It has to be noted that the prediction of the emission spectra itself is a much more demanding task.

When applying a similar approach to get a simple understanding of mode propagation in oxide-confined VCSELs, the main difficulty is the identification of a suitable refractive index profile in the planar cavity. The vital role that is played by the oxide layer can be inferred from the reduction of its refractive index from about 3.0 before to only $\bar{n}_{\mathrm{ox}} \approx 1.6$ after selective oxidation [48]. The local index decrease leads to a blue-shift $\Delta\lambda_{\mathrm{ox}} < 0$ of the cavity resonance wavelength in the oxidized section with respect to the active device center. The wavelength shift can be easily determined from transfer matrix calculations and be translated into an average cavity index variation

$$\Delta\bar{n}_{\mathrm{c}} = \langle\bar{n}\rangle\Delta\lambda_{\mathrm{ox}}/\lambda\ , \tag{41}$$

where λ and $\langle\bar{n}\rangle$ denote the resonance wavelength and average refractive index before oxidation [49]. In this way, we have used a perturbation-like approach to convert the inhomogeneous index profile into that of a homogeneous step-index fiber.

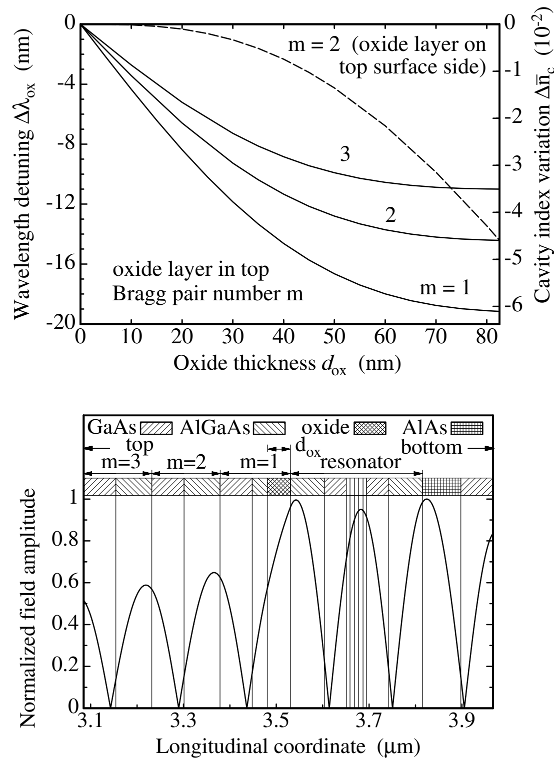

Fig. 17. Resonance wavelength detuning and corresponding cavity index variation versus thickness of the oxide layer that is located in the m-th Bragg pair of the VCSEL top mirror. The dashed line for $m = 2$ assumes an oxide layer starting at the node of the electric field. The virtual standing-wave pattern in the oxidized cavity section is illustrated in the lower part for $d_{\mathrm{ox}} = 50\,\mathrm{nm}$ and $m = 1$

Figure 17 shows calculated index variations for a model 980 nm VCSEL with different thickness d_{ox} and position of the oxide layer. Due to the exponential-like shaped envelope of the longitudinal standing-wave pattern

in Fig. 6, the detuning decreases with increasing distance from the active layers. Induced cavity index variations likewise are larger when the oxide layer is located closer to an antinode of the electric field. On the other hand, placing the aperture right at a field node creates a weakly index-guided waveguide while still providing ideal current confinement. Intuitively it is clear that such a configuration should favor transverse singlemode emission of a VCSEL, which has indeed been proven experimentally [12]. Due to restrictions from oxidation technology and voltage breakdown behavior, the minimum oxide thickness is limited to 10 to 30 nm. Even with $d_{\mathrm{ox}} = 30\,\mathrm{nm}$, cavity index steps $|\Delta\bar{n}_{\mathrm{c}}|$ of just a few times 10^{-3} can be obtained. Weak index-guiding designs and appropriate choice of active size have led to singlemode VCSELs like in Fig. 11 with output powers in the few mW range.

The conversion of the longitudinally inhomogeneous refractive index profile of a VCSEL into that of a homogeneous quadratic or step-index waveguide also easily allows estimations of the transverse mode spacing $\Delta\lambda_{lp}$. From the propagation constant [50]

$$\beta_{lp} \approx \frac{2\pi\bar{n}_0}{\lambda}\left(1 - \frac{2p+l-1}{2\pi}\,\frac{\lambda}{a}\,\frac{\sqrt{\bar{n}_0^2 - \bar{n}_a^2}}{\bar{n}_0^2}\right) \tag{42}$$

of a weakly guided mode in a quadratic index medium one expects a proportionality $\Delta\lambda_{lp} \propto \lambda^2/D_{\mathrm{a}}$, whereas a step-index guide can even lead to $\Delta\lambda_{lp} \propto \lambda^3/D_{\mathrm{a}}^2$ [51]. In the first case, the characteristic profile diameter $2a$ is assumed to scale with the active diameter as $2a \propto D_{\mathrm{a}}$. As seen in Fig. 11, transverse mode spacings of small diameter VCSELs can easily exceed 1 nm. In the emission spectrum, the influence of thermally induced index guiding is indicated by an increase of mode spacing with current. It should be added that any deviation of the refractive index profile (including the gain profile of the active layer) from the assumed symmetry, tracing back to, e.g., processing tolerances, induced stress, or built-in strain can break the degeneracy of modes with respect to both orientation and polarization, resulting in a more complex transverse mode spectrum.

4 Dynamic and Noise Behavior

Applications of VCSELs in data transmission systems rely on the dynamic and noise properties of the source. These characteristics are generally obtained from rate equations [2], [3] describing the interaction of electrons and photons in the laser cavity. Dynamic behavior is most easily inferred from the small-signal current modulation transfer function. Noise originates from spontaneous emission whose statistic nature is expressed in the rate equations by Langevin forces for carriers and photons, especially leading to the relative intensity noise spectrum. For simplicity we will mostly restrict ourselves to singlemode laser oscillation.

4.1 Rate Equations

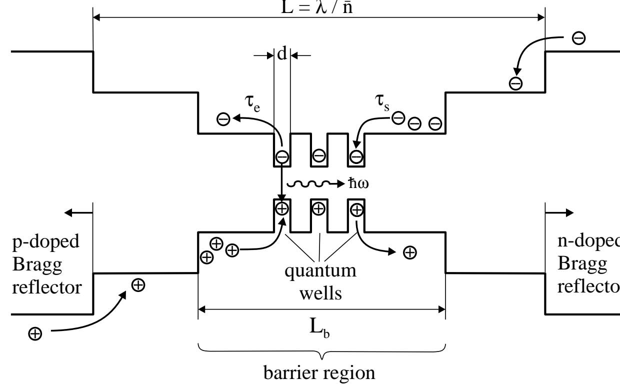

Fig. 18. Dynamic model of a VCSEL active region, indicating electron injection into barriers as well as diffusion into and escape from the QWs

A widely accepted treatment of laser dynamics [52], illustrated in Fig. 18, describes the interaction of three different kinds of particle reservoirs in the device, namely carriers of densities n_w in the active QW region and n_b in the adjacent barriers with volumes V_w and V_b, respectively, and photons of density N in the resonator with photon volume V_p. Particle densities are taken as spatial averages over their corresponding volumes. In a VCSEL, the active layer is composed of a few QWs of total thickness d_a, the barriers often extend over the inner half-wavelength thick part of the cavity, and the resonator of length L_eff contains the, e.g., one-wavelength thick cavity and the penetration depths into both Bragg mirrors, as discussed before. The ratio

$$\frac{V_\mathrm{w}}{V_\mathrm{p}} = \varGamma = \varGamma_z \cdot \varGamma_\mathrm{t} = \frac{d_\mathrm{a}}{L_\mathrm{eff}} \cdot \varGamma_\mathrm{t} \tag{43}$$

between the active and photon volumes is denoted as confinement factor $\varGamma$, which can be split into a longitudinal and transverse part, where the latter is limited to $0 < \varGamma_\mathrm{t} \leq 1$ and often can be approximated by $\varGamma_\mathrm{t} \approx 1$. If we allow for a moment the existence of different transverse modes of mode order m, the rate equations for time derivatives $\mathrm{d}/\mathrm{d}t$ are written as

$$\frac{\mathrm{d}n_\mathrm{w}}{\mathrm{d}t} = \frac{n_\mathrm{b}}{\tau_\mathrm{s}}\frac{V_\mathrm{b}}{V_\mathrm{w}} - \frac{n_\mathrm{w}}{\tau_\mathrm{e}} - \frac{n_\mathrm{w}}{\tau_\mathrm{sp,w}} - \varGamma_\mathrm{r} v_\mathrm{gr} \sum_m g_m(n_\mathrm{w}, N) N_m + F_n(t) \ , \tag{44a}$$

$$\frac{\mathrm{d}n_\mathrm{b}}{\mathrm{d}t} = \frac{n_\mathrm{w}}{\tau_\mathrm{e}}\frac{V_\mathrm{w}}{V_\mathrm{b}} - \frac{n_\mathrm{b}}{\tau_\mathrm{s}} - \frac{n_\mathrm{b}}{\tau_\mathrm{sp,b}} + \frac{\eta_I I}{q V_\mathrm{b}} \ , \tag{44b}$$

$$\frac{\mathrm{d}N_m}{\mathrm{d}t} = \bar{\beta}_{\mathrm{sp},m} \varGamma_m \frac{n_\mathrm{w}}{\tau_\mathrm{sp,w}} - \frac{N_m}{\tau_{\mathrm{p},m}} + \varGamma_m \varGamma_\mathrm{r} g_m(n_\mathrm{w}, N) v_\mathrm{gr} N_m + F_N(t) \ , \tag{44c}$$

where Langevin forces $F_n(t)$ for electron density and $F_N(t)$ for photon density have been added to account for the statistical nature of spontaneous

emission events that are responsible for laser noise [2], [3]. The time dependence of particle densities is described by several time constants τ. Carriers in the well are supplied from the barriers with τ_s, which can be interpreted as transport time and is dominated by diffusion in undoped potential wells [52]. Carriers escape from the wells into the barriers with τ_e and are removed from both regions by spontaneous emission with time constants $\tau_\mathrm{sp,w}$ and $\tau_\mathrm{sp,b}$, respectively. Carriers are injected into the barriers by the external current I, where we encounter the injection efficiency η_I already introduced in (24).

The photon density of the considered mode is increased by spontaneous emission according to the spontaneous emission factor $\bar{\beta}_\mathrm{sp}$ [53] and decreases due to optical losses and outcoupling, both included in the photon lifetime τ_p. With the relative confinement factor Γ_r from Sect. 2.1, the stimulated emission terms in (44a) and (44c) take the spatial overlap between the QWs with material gain g and the standing-wave pattern in the resonator into account.

For the following discussion it is sufficient to restrict ourselves to the important case of single transverse mode emission, greatly simplifying the system of rate equations. The modal material gain coefficient of the QWs at the spectral position of the lasing mode, which for VCSELs in general is not identical to the peak gain (see Fig. 13), is then approximated by [54]

$$g(n_\mathrm{w}, N) = \frac{\bar{g}\ln(n_\mathrm{w}/n_\mathrm{wt})}{1+\varepsilon N} \tag{45}$$

with the gain constant $\bar{g}$ and the transparency carrier density n_wt, depending (for constant temperature) on the QW thickness and materials used. Gain compression [55] due to effects like spectral hole burning, carrier heating, or spatial hole burning is accounted for by the parameter ε.

4.2 Small-Signal Modulation Response

From the rate equations we can infer the dynamic response of the VCSEL to a harmonic variation $\Delta I(t)$ of the current about an operating point $I_0 \gg |\Delta I(t)|$. Equations are first of all linearized with respect to the resulting variations $\Delta n_\mathrm{w}(t)$, $\Delta n_\mathrm{b}(t)$, and $\Delta N(t)$ which are all small compared to n_w0, n_b0, and N_0, respectively, and after that Fourier transformed into quantities $\Delta\widetilde{I}(\nu)$, etc. to obtain the spectral fluctuations as a function of frequency ν. The carrier dependent part of the gain coefficient (45) is also linearized to the form

$$g(n_\mathrm{w0}) = \bar{g}\ln\left(\frac{n_\mathrm{w0}}{n_\mathrm{wt}}\right) \approx \bar{a}\,(n_\mathrm{w0} - n_\mathrm{t}) \tag{46}$$

with differential gain coefficient $\bar{a}$ and transparency carrier density n_t expressed as

$$\bar{a} = \frac{\bar{g}}{n_\mathrm{w0}} \qquad \text{and} \qquad n_\mathrm{t} = n_\mathrm{w0}\left(1 - \ln\left(\frac{n_\mathrm{w0}}{n_\mathrm{wt}}\right)\right) . \tag{47}$$

Langevin forces F_n, F_N are both set to zero since noise is not of interest here. Neglecting the spontaneous emission contributions in (44b) and (44c) owing to the small magnitude of $\bar{\beta}_{\rm sp}$ [53], the resulting modulation transfer function that relates the photon density fluctuations to those of the modulating current is finally obtained as

$$M(\nu) = \frac{\Delta\widetilde{N}(\nu)}{\Delta\widetilde{I}(\nu)/q} = \frac{1}{1+\mathrm{i}2\pi\nu\tau_{\rm s}}\,\frac{A}{4\pi^2(\nu_{\rm r}^2-\nu^2)+\mathrm{i}2\pi\gamma\nu} \tag{48}$$

with the amplitude factor

$$A = \frac{\eta_I v_{\rm gr}\Gamma_{\rm r}\bar{a}N_0}{V_{\rm p}\chi(1+\varepsilon N_0)}\ , \tag{49}$$

the damping coefficient

$$\gamma = \frac{1}{\chi\tau_{\rm sp,w}} + AV_{\rm p} + \frac{\varepsilon N_0}{\tau_{\rm p}(1+\varepsilon N_0)}\ , \tag{50}$$

and the resonance frequency

$$\nu_{\rm r} = \frac{1}{2\pi}\sqrt{A\,\frac{V_{\rm p}}{\tau_{\rm p}}\left(1+\frac{\varepsilon}{\tau_{\rm sp,w}v_{\rm gr}\Gamma_{\rm r}\bar{a}}\right)} \approx \frac{1}{2\pi}\sqrt{A\,\frac{V_{\rm p}}{\tau_{\rm p}}}\ , \tag{51}$$

where additionally the transport factor

$$\chi = 1 + \frac{\tau_{\rm s}}{\tau_{\rm e}} \tag{52}$$

has been introduced. The damping coefficient can be rewritten as

$$\gamma = K\nu_{\rm r}^2 + \frac{1}{\chi\tau_{\rm sp,w}} \tag{53}$$

with the so-called K-factor

$$K = 4\pi^2\left(\tau_{\rm p} + \frac{\varepsilon}{v_{\rm gr}\Gamma_{\rm r}\bar{a}/\chi}\right)\ . \tag{54}$$

Its importance arises from the fact that the maximum 3-dB modulation corner frequency of $|M(\nu)|^2$ is related to K as [56]

$$\nu_{\rm max} = \sqrt{2}\,\frac{2\pi}{K}\ , \tag{55}$$

indicating the intrinsic modulation limit of the laser without any parasitic effects. The K-factor is usually determined by plotting the damping coefficient (53) as a function of the resonance frequency squared, where both γ and $\nu_{\rm r}$ are obtained from curve fits to the measured data according to (48), as illustrated in Fig. 19. For the fits, mostly $2\pi\nu\tau_{\rm s} \ll 1$ is assumed. In fact, at least for the frequency range up to 15 GHz, carrier transport seems not to be a speed limiting effect.

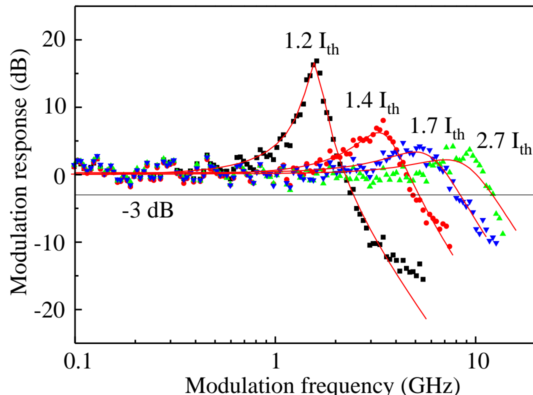

Fig. 19. Measured modulation transfer function $|M(\nu)|^2$ of a singlemode oxidized VCSEL for different currents above threshold current $I_{\rm th} = 1.1\,{\rm mA}$ [57]. Solid lines are curve fits according to (48), assuming $2\pi\nu\tau_{\rm s} \ll 1$

Smallest K-factors observed for VCSELs so far are in the 0.15 to 0.2 ns range [58], [59] and 3-dB small-signal modulation bandwidths exceed 20 GHz [58]. Limiting effects are self-heating and the onset of multi-transverse mode operation, where in the latter case power partition between the modes limits their individual photon densities. To further push the internal frequency damping limit, the K-factor has to be minimized, for which case a corresponding design rule can easily be derived. We start by writing the photon lifetime as $\tau_{\rm p} = (\Gamma\Gamma_{\rm r} g_{\rm th} v_{\rm gr})^{-1}$ in accordance with (15) or as obtained from (44c) when putting $d/dt = 0$ and neglecting spontaneous emission as well as the noise source. Recalling $\bar{a} = \bar{g}/n_{\rm th}$ with the threshold carrier density $n_{\rm th} = n_{\rm w0}$ shows that there exists an optimum threshold gain $g_{\rm th}$ that minimizes K. Rearranging (46) as $n_{\rm th} = n_{\rm wt} \exp\{g_{\rm n}\}$ with normalized threshold gain $g_{\rm n} = g_{\rm th}/\bar{g}$ leads to the characteristic equation $\Gamma\varepsilon\chi n_{\rm wt} g_{\rm n}^2 = \exp\{-g_{\rm n}\}$, from which $g_{\rm n}$ can be obtained numerically. The minimum K-factor then results as

$$K_{\rm min} = \frac{4\pi^2}{v_{\rm gr}\Gamma\Gamma_{\rm r}\bar{g}} \frac{g_{\rm n}+1}{g_{\rm n}^2} = 4\pi^2\tau_{\rm p}\left(1 + \frac{\bar{g}}{g_{\rm th}}\right) . \qquad (56)$$

Fig. 20 shows calculated values of $g_{\rm n}$, $K_{\rm min}$, and $\nu_{\rm max}$ for a reasonable interval of the gain compression factor ε, assuming parameters $\Gamma_{\rm t} = 1$, a 3 QW gain region with $d_{\rm a} = 24\,{\rm nm}$ and $\Gamma_{\rm r} = 1.8$, $L_{\rm eff} = 1.25\,\mu{\rm m}$, $\chi = 1$, as well as $v_{\rm gr} = c/3.6$. As active layer, both InGaAs QWs with $n_{\rm wt} = 1.8 \cdot 10^{18}\,{\rm cm}^{-3}$, $\bar{g} = 2100\,{\rm cm}^{-1}$ and GaAs QWs with $n_{\rm wt} = 2.6 \cdot 10^{18}\,{\rm cm}^{-3}$, $\bar{g} = 2400\,{\rm cm}^{-1}$ [3] have been considered.

It is seen that for smaller gain compression ε, the optimum threshold gain increases, leading to a smaller K-factor and higher bandwidth, with the strained InGaAs QW system being slightly more advantageous. For $\varepsilon = 7 \cdot 10^{-18}\,{\rm cm}^3$ with $g_{\rm n} \approx 1$, the two terms of the sum in (54) or (56) contribute almost equally to the total K, whereas for higher ε the term corresponding to the gain nonlinearity prevails. The preceding discussion has shown that, equivalent to EELs [55], the optimum VCSEL cavity design for high-speed

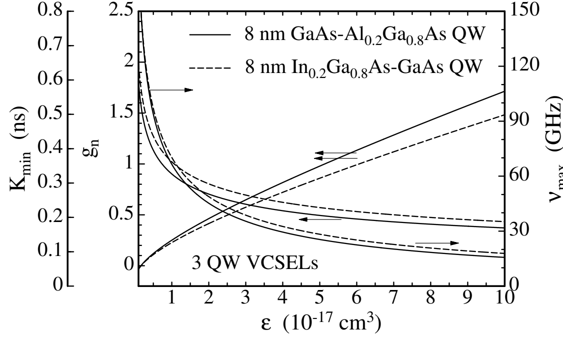

Fig. 20. Optimum normalized threshold gain g_n, minimum K-factor K_min, and corresponding modulation bandwidth ν_max versus gain compression factor ε for GaAs and InGaAs 3 QW VCSELs

operation is closely related to nonlinear gain properties of the active layer, which have thus to be taken into account to obtain maximum internal modulation capability of the device.

For applications in optical communications, one is generally interested to obtain high modulation bandwidths for small operating currents. Taking the approximation for ν_r in (51), neglecting gain compression as well as carrier transport, and relating the photon density N_0 to the output power P as $\eta_\mathrm{d} N_0 V_\mathrm{p} \hbar\omega = \tau_\mathrm{p} P$, we obtain the expression

$$\nu_\mathrm{r} \approx \frac{1}{2\pi}\sqrt{\frac{v_\mathrm{gr}\Gamma_\mathrm{r}\bar{a}P}{\hbar\omega\eta_\mathrm{d}V_\mathrm{p}}} = \frac{1}{2\pi}\sqrt{\frac{\eta_I v_\mathrm{gr}\Gamma_\mathrm{r}\bar{a}}{qV_\mathrm{p}}}\cdot\sqrt{I-I_\mathrm{th}} = M_\mathrm{r}\cdot\sqrt{I-I_\mathrm{th}}\;, \quad (57)$$

where furthermore (23) and (24) have been used. As a figure of merit, the modulation current efficiency factor (MCEF) is often given to specify the increase of the 3-dB corner frequency of $|M(\nu)|^2$ as

$$\mathrm{MCEF} = \frac{\nu_{3\,\mathrm{dB}}}{\sqrt{I-I_\mathrm{th}}}\;. \quad (58)$$

In the case of sufficiently low damping with $\gamma^2 \ll 8\pi^2\nu_\mathrm{r}^2$, one would expect a relation $\mathrm{MCEF} \approx \sqrt{1+\sqrt{2}}\,M_\mathrm{r} \approx 1.55\,M_\mathrm{r}$ which is usually not observed in practice (see, e.g., [58]). It is important to note from (57) that one should keep the differential gain high and the cavity volume $V_\mathrm{p} = L_\mathrm{eff}A_\mathrm{a}$ low in order to maximize the modulation efficiency. MCEFs exceeding $14\,\mathrm{GHz}/\sqrt{\mathrm{mA}}$ have already been reported [58], indicating that VCSELs can achieve modulation speeds in the multi-GHz regime even if driven only slightly above threshold.

Deviations from an ideal damping-limited modulation behavior especially occur due to parasitic elements found in the laser equivalent electric circuit and can be accounted for by a parasitic modulation transfer function, converting $M(\nu)$ from (48) into the total response

$$M_\mathrm{tot}(\nu) = M(\nu)\cdot M_\mathrm{par}(\nu)\;. \quad (59)$$

Even if bondwire and track inductances and bondpad capacitances are kept low, the RC lowpass filter composed of the ohmic series resistance and the

capacitance related to the etched mesa in oxide-confined VCSELs can impose a serious frequency limit. In this simple case $M_{\mathrm{par}}(\nu)$ is just expressed as $(1+\mathrm{i}2\pi\nu\tau_{RC})^{-1}$. Elements of the equivalent circuit can conveniently be deduced from microwave impedance measurements [58], [57]. The influence of M_{par} also leads to a correspondence between M_{r} from (57) and the MCEF other than mentioned above.

4.3 Relative Intensity Noise

The spectral relative intensity noise (RIN) relates the photon density fluctuations to the mean photon density squared as [60]

$$\mathrm{RIN}(\nu) = 2\,\frac{\langle|\Delta\widetilde{N}(\nu)|^2\rangle}{\langle N\rangle^2} = 2\,\frac{\langle|\Delta\widetilde{P}(\nu)|^2\rangle}{\langle P\rangle^2} = 2\,\frac{\langle|\Delta\widetilde{I}_{\mathrm{PD}}(\nu)|^2\rangle}{\langle I_{\mathrm{PD}}\rangle^2}\,, \tag{60}$$

where the angular brackets denote an average over the observation time and $\mathrm{RIN}(\nu)$ is measured in dB/Hz. In (60) we have furthermore used the proportionality between spectral components of photon density $\Delta\widetilde{N}(\nu)$, output power $\Delta\widetilde{P}(\nu)$, and detector photocurrent $\Delta\widetilde{I}_{\mathrm{PD}}(\nu)$ and correspondingly for the mean values $\langle N\rangle$, $\langle P\rangle$, and $\langle I_{\mathrm{PD}}\rangle$. In contrast to the previous section, we assume the photon density to be modulated here by spontaneous emission processes, whereas current density fluctuations can be neglected. Thus, putting $\Delta\widetilde{I}(\nu) = 0$ after linearization and Fourier transformation of (44a)–(44c) and inserting proper expressions [3] for the Langevin forces F_n, F_N leads to the result

$$\mathrm{RIN}(\nu) = \frac{4\bar{\beta}_{\mathrm{sp}}\Gamma n_{\mathrm{w0}}}{\tau_{\mathrm{sp,w}}\langle N\rangle}\,\frac{4\pi^2\nu^2+\gamma^{*2}}{16\pi^4(\nu_{\mathrm{r}}^2-\nu^2)^2+4\pi^2\gamma^2\nu^2} \tag{61}$$

with the modified damping coefficient

$$\gamma^* = \gamma - \frac{\varepsilon\langle N\rangle}{\tau_{\mathrm{p}}(1+\varepsilon\langle N\rangle)} \approx \frac{1}{\chi\tau_{\mathrm{sp,w}}} + 4\pi^2\nu_{\mathrm{r}}^2\tau_{\mathrm{p}}\,, \tag{62}$$

where we have used (50) and the approximation in (51) to obtain the expression on the right-hand side of (62) and more appropriately have written $\langle N\rangle$ instead of N_0 in conjunction with noise processes. Other than the modulation transfer function (48), $\mathrm{RIN}(\nu)$ does not explicitly include carrier transport effects in a lowpass-like prefactor $(1+\mathrm{i}2\pi\nu\tau_{\mathrm{s}})^{-1}$. Relative intensity noise measurements can therefore be employed to characterize intrinsic dynamic properties of laser diodes.

For small resonance frequencies we can approximate $\gamma^* \approx (\chi\tau_{\mathrm{sp,w}})^{-1}$ in (62) to obtain a decrease of RIN according to

$$\mathrm{RIN}(\nu) \propto \langle N\rangle^{-3} \propto \langle P\rangle^{-3} \qquad \text{for } \nu \ll \nu_{\mathrm{r}}\,, \tag{63}$$

since $\nu_{\mathrm{r}}^2 \propto \langle N\rangle$ for $\varepsilon\langle N\rangle \ll 1$. For large ν_{r}, i.e., far above threshold, we can neglect $(\chi\tau_{\mathrm{sp,w}})^{-1}$ in (62), and the RIN only decreases as

$$\mathrm{RIN}(\nu) \propto \langle N\rangle^{-1} \propto \langle P\rangle^{-1}\,. \tag{64}$$

In the above treatment we have not considered that the emitted wave consists of single quanta of energy $\hbar\omega$, which, for thermal or ideally coherent radiation, are distributed according to Poisson's statistics. In other words, we have to include the well known fact that the quantum nature of light is the cause of the shot noise contribution in the photodetector, leading to a quantum noise limit of the RIN according to

$$\mathrm{RIN_Q} = \frac{2q}{\langle I_{\mathrm{PD}} \rangle} = \frac{2\hbar\omega}{\eta_{\mathrm{PD}} \langle P \rangle} \tag{65}$$

with the detection efficiency η_{PD}. Concerning RIN measurements with a pin-photodiode, we have to add the term (65) to the classical expression (61). For a mean photocurrent $\langle I_{\mathrm{PD}} \rangle = 1\,\mathrm{mA}$, the quantum noise limit is found at $-155\,\mathrm{dB/Hz}$ and can fall below only for non-Poissonian (squeezed) light [61]. It is now seen that the dependence $\mathrm{RIN}(\nu) \propto \langle P \rangle^{-1}$ has to be considered as a fundamental limit although it was earlier obtained for a rather special case.

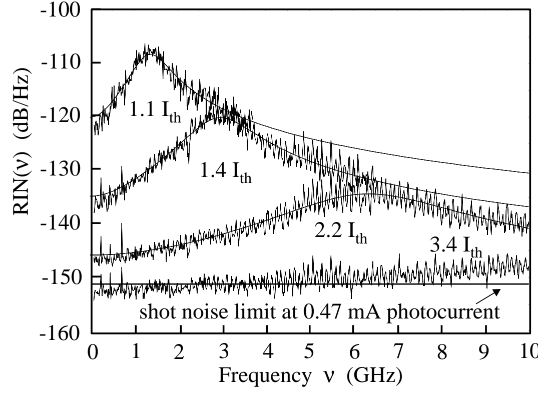

Fig. 21. Measured RIN spectra of a singlemode, single-polarization oxide-confined VCSEL for different pumping levels above threshold current $I_{\mathrm{th}} = 0.5\,\mathrm{mA}$. The measurement system noise level is 2.5 dB below the shot noise level for 0.47 mA photocurrent. Theoretical curves are drawn as solid lines

The predicted spectral behavior of the RIN is experimentally observed for singlemode VCSELs with high side-mode suppression, as indicated in Fig. 21 [62]. Above threshold, the noise level rapidly decreases with increasing current and the resonance frequency is shifted beyond 10 GHz. At a current of only 1.7 mA, corresponding to 1 mW optical output power, the shot noise level of the detecting system is reached over almost the whole frequency interval from 0 to 10 GHz. For still higher currents, higher order modes start to oscillate and mode competition severely increases the laser noise. Deteriorations of the RIN spectrum are also observed if lasing on the orthogonally polarized fundamental mode sets in.

When dealing with digital optical data transmission, the instantaneous temporal fluctuations of the signal are usually of interest. By writing $P(t) = \langle P \rangle + \delta P(t)$ for the optical power and $I_{\mathrm{PD}} = \langle I_{\mathrm{PD}} \rangle + \delta I_{\mathrm{PD}}(t)$ for the photocurrent, where $\langle \delta P(t) \rangle = \langle \delta I_{\mathrm{PD}}(t) \rangle = 0$, we can express the relative temporal

variations of the signal or its relative variance through the relative intensity noise integrated over the system bandwidth $\Delta\nu_s$ as

$$\mathrm{IRIN} = \int_0^{\Delta\nu_s} \mathrm{RIN}(\nu)\,\mathrm{d}\nu = \frac{\langle \delta P^2(t)\rangle}{\langle P\rangle^2} = \frac{\langle \delta I_{\mathrm{PD}}^2(t)\rangle}{\langle I_{\mathrm{PD}}\rangle^2}\ . \tag{66}$$

4.4 Emission Linewidth

It is well known [63], [2], [3] that statistical phase fluctuations of the electric field introduced by spontaneous emission processes are responsible for the finite linewidth of laser diode oscillation. The spectral power density of a singlemode laser emission line is well approximated by the Lorentzian lineshape function

$$|\widetilde{E}(\nu)|^2 = |\widetilde{E}(\nu_m)|^2 \,\frac{(\Delta\nu_{\mathrm{L}}/2)^2}{(\Delta\nu_{\mathrm{L}}/2)^2 + (\nu-\nu_m)^2} \tag{67}$$

with ν_m denoting the center frequency of the mode and $\Delta\nu_{\mathrm{L}}$ is the full linewidth at half maximum. The linewidth is given by

$$\Delta\nu_{\mathrm{L}} = \frac{\bar{\beta}_{\mathrm{sp}}\Gamma\langle n_{\mathrm{w}}\rangle}{4\pi\tau_{\mathrm{sp,w}}\langle N\rangle}\,(1+\alpha_{\mathrm{H}}^2)\ , \tag{68}$$

where α_{H} is the linewidth enhancement factor that has also been determined for VCSELs [64] and typically takes values between -2 and -7.

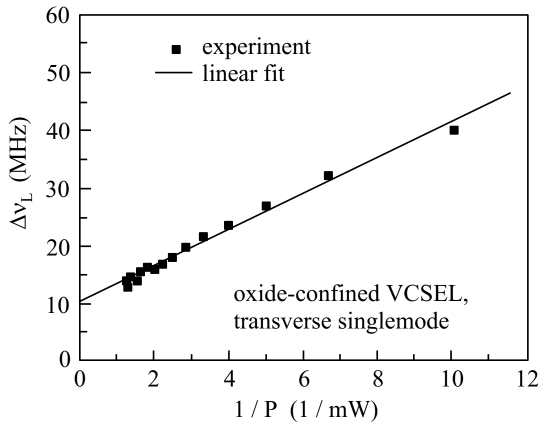

Fig. 22. Singlemode VCSEL emission linewidth as a function of inverse output power

Figure 22 shows measured linewidths for a singlemode oxide-confined VCSEL of about 4 µm diameter. As expected from (68), the linewidth increases linearly with inverse output power. However, a residual linewidth of $\Delta\nu_0 = 11\,\mathrm{MHz}$ is observed for the extrapolation $P \to \infty$, which is attributed to mode competition with not perfectly suppressed side-modes or perhaps

$1/f$-noise contributions, similarly to EELs [60]. Considering the experimentally found residual linewidth $\Delta\nu_0$, relation (68) is rewritten as

$$\Delta\nu_{\mathrm{L}}^{*} = \Delta\nu_{\mathrm{L}} + \Delta\nu_0 \ . \qquad (69)$$

The onset of higher transverse order modes at higher currents generally leads to an increase of the fundamental mode linewidth due to reduction of modal power, although the total power is still increasing. Lowest linewidths obtained with VCSELs to date are in the few-MHz range. Due to their convenient, mode-hopping free tunability via the operating current and sufficiently low linewidths, singlemode VCSELs are good candidates for spectroscopic applications or gas sensing, with oxygen sensors operating in the 760 nm wavelength region as a prominent example [65].

5 VCSEL Based Optical Interconnects

In this section we will discuss some aspects of VCSEL applications in optical interconnects and illustrate selected results of data transmnission experiments. Among the attractive features of VCSELs for short-distance fiber transmission are low driving power, high-speed current modulation for multi-Gbit/s data generation, simple mounting technology related to the pigtailing of light emitting diodes, and parallel arrangements in one- or two-dimensional arrays. The performance of data links is commonly characterized by bit error rate (BER) measurements [2], [66]. Stringent demands for BERs of less than 10^{-12} or even down to 10^{-15} are required in computer interconnects. High aggregate bitrates are most easily achieved with parallel links making use of optical fiber ribbons, where bitrates of individual channels currently are in the 2.5 Gbit/s range [67] and will soon reach 10 Gbit/s [68]. Since their emission wavelength can be adjusted during epitaxial growth, VCSELs are well suited for wavelength division multiplexing transmission [69], nowadays extensively exploited in optical telecommunications. For reasons of manufacturing cost, this advanced technique is expected to be unleashed in future generations of short-distance interconnect modules. Cost effectiveness is also the driving force behind the revival of graded-index multimode fiber waveguiding for transmission distances in the few 100 m range.

5.1 Fiber Coupling

A favorable property of VCSEL-based optical interconnect systems is the high efficiency power launching capability into optical fibers. Often, quasi or direct butt coupling techniques can be employed, taking advantage of the circularly symmetric emission profile and resulting in low cost solutions by avoiding external optics. Assuming Gaussian field distributions $E(r) \propto$

$\exp\{-(r/w_{\mathrm{l,f}})^2\}$ for both the laser and the fiber with spot radii w_l and w_f, respectively, leads to a power coupling efficiency of

$$\eta_\mathrm{fc} = \frac{4w_\mathrm{l}^2 w_\mathrm{f}^2}{(w_\mathrm{l}^2 + w_\mathrm{f}^2)^2} \ , \tag{70}$$

where possible Fresnel reflection losses have not been taken into account. For a standard singlemode fiber with $2w_\mathrm{f} = 9\,\mu\mathrm{m}$, one expects coupling efficiencies exceeding 50 % for singlemode VCSEL spot diameters $2w_\mathrm{l} \geq 3.8\,\mu\mathrm{m}$ or $\eta_\mathrm{fc} > 80\,\%$ for $2w_\mathrm{l} \geq 5.6\,\mu\mathrm{m}$. In these examples, no upper limits have been specified due to multimode emission tendency for large active diameters. Also it has to be noted that the specified fiber carries two guided LP modes in the wavelength range between 800 and 1000 nm discussed in this chapter, so that special measures like fiber mode filtering have to be taken in order to avoid intermodal dispersion limitations [70]. For sufficiently stable coupling arrangements, index matching or fiber anti-reflection coating do not necessarily have to be applied with up to few 10 µm wide air gaps, since the fiber endface only slightly alters the properties of the highly reflective outcoupling mirror and thus the VCSEL threshold. This issue is tightly related to the feedback insensitive operation behavior observed for VCSELs [71], [72]. Experimentally, butt coupling at $\lambda = 980\,\mathrm{nm}$ from proton-implanted VCSELs of about 4 µm spot diameter into true singlemode fiber of 4.5 µm core diameter has been investigated, yielding coupling efficiencies of larger than 80 % [73]. For coupling from singlemode VCSEL into graded-index multimode fiber with 50 µm core diameter and a numerical aperture of 0.2, $\eta_\mathrm{fc} > 80\,\%$ can be easily obtained. Multimode sources can show reduced fiber coupling efficiencies and increased sensitivity to external feedback caused by the fiber endface [74].

5.2 Large-Signal Modulation Effects

Concerning the dynamic behavior, we have discussed small-signal modulation in the previous section. However, for digital modulation, large-signal effects come into play, which have to be considered for system design. To analyze large-signal behavior, the complete system of time dependent rate equations (44a)–(44c) has to be taken into account and perhaps even to be extended to include lateral variations of particle densities as well as carrier diffusion. For systems employing singlemode VCSELs, mainly three effects have an impact on the modulation perfomance and have been investigated experimentally in [57]. As the first one, *turn-on delay* occurs if the VCSEL is biased below threshold and time is taken to build up the threshold carrier density in the active layer. Especially for bias-free operation [75], turn-on delays exceeding 100 ps are easily observed. In general, low threshold properties of VCSELs are very advantageous and bias-free data transmission at 2.5 Gbit/s data rate over 500 m of multimode fiber has been demonstrated [76] (see Fig. 23). *Turn-on jitter* as the standard deviation of the turn-on delay is caused by

fluctuations due to spontaneous emission and is found to be in the 10 ps range for singlemode VCSELs, thus imposing no limit even for 10 Gbit/s systems. Finally, so-called *pattern effects* that are due to memory-like behavior of the carrier reservoir and that result in cavity build-up time variations play a major role in practice, even for bias points above threshold. To minimize bit pattern effects, it is desirable to have high-speed VCSEL response, i.e., high resonance frequencies in both the logical on- and off-states. Unfortunately, this rule interferes with the demand for high extinction ratios in the optical signal, so that optimum operation conditions have to be chosen.

It has to be mentioned that also the noise behavior can be quite different for large-signal modulation, especially if transverse modes of different order or polarization are only weakly suppressed and mode competition comes into play.

5.3 High-Speed Optical Data Transmission

In digital optical transmission, the BER is expressed as a function of the noise related relative level separation Q through the well known formula [2]

$$\mathrm{BER} \approx \frac{1}{\sqrt{2\pi}Q}\exp\left\{-\frac{Q^2}{2}\right\}\left(1-\frac{1}{Q^2}\right) \tag{71}$$

which is valid for Gaussian statistics of the logic level fluctuations. Denoting the variance of the photocurrent noise fluctuations by $\langle \delta I_{\mathrm{PD}}^2 \rangle$, the parameter Q is written as

$$Q = \frac{\eta_{\mathrm{e}}\eta_{\mathrm{PD}}\langle P\rangle/(\hbar\omega)}{\sqrt{\langle \delta I_{\mathrm{PD}}^2\rangle}/q} = \eta_{\mathrm{e}}\,\frac{\langle I_{\mathrm{PD}}\rangle}{\sqrt{\langle \delta I_{\mathrm{PD}}^2\rangle}} = \frac{\eta_{\mathrm{e}}}{\sqrt{\mathrm{IRIN}}}\,, \tag{72}$$

where the integrated RIN from (66) has been used, and $\eta_{\mathrm{e}} = (1-r_{01})/(1+r_{01})$ denotes an extinction efficiency of the optical signal, with $r_{01} = \langle I_0\rangle/\langle I_1\rangle$ being the ratio between average photocurrents in the off- and on-state. Vanishing modulation depth results in $\eta_{\mathrm{e}} = 0$, whereas $\eta_{\mathrm{e}} = 1$ is obtained for modulation down to the threshold current. Combining (71) and (72) gives a characteristic relation between BER and average received power $\langle P\rangle$, which is often graphically illustrated by properly adjusting the ordinate in order to nominally obtain a straight line. Especially for $Q \gg 1$ we get the simple relationship

$$\mathrm{BER} \approx \frac{1}{\eta_{\mathrm{e}}}\sqrt{\frac{\mathrm{IRIN}}{2\pi}}\exp\left\{-\frac{\eta_{\mathrm{e}}^2}{2\,\mathrm{IRIN}}\right\} \tag{73}$$

between the bit error rate and the intensity noise.

Figure 23 summarizes the BER performance obtained for various singlemode VCSEL links employing multimode fiber (MMF) or singlemode fiber (SMF), all showing quasi error-free operation with BERs in the 10^{-11} range without indication of error floors. The combination of singlemode VCSEL and

MMF has been discussed quite controversially due to modal noise related issues, and often the use of low coherence multimode VCSELs is suggested [77], [78]. However, at least for point-to-point interconnects or if small mode selective transmission loss is present, noise performance of fiber interconnects with SM VCSELs is found to be superior to those with MM sources simply because mode competition noise in the laser does not occur. The large mode field mismatch moreover may lead to notably decreased sensitivity with regard to distant optical feedback [72].

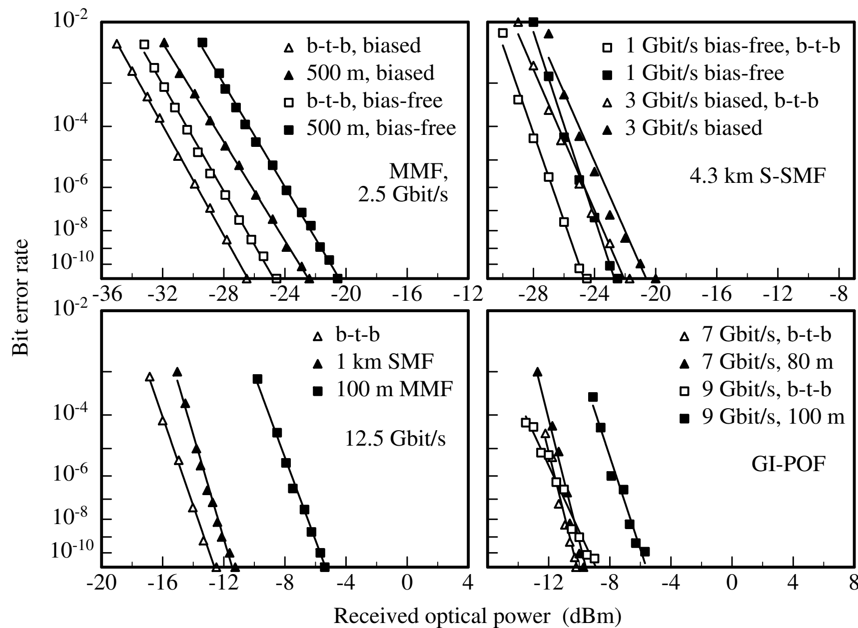

Fig. 23. Bit error rate performance as a function of received optical power for data transmission with oxide-confined singlemode VCSELs over various types of fiber as well as corresponding back-to-back (b-t-b) measurements. **Top left:** Biased and bias-free 2.5 Gbit/s transmission over 500 m MMF at 840 nm [76]. **Top right:** 3 Gbit/s biased and 1 Gbit/s bias-free transmission over 4.3 km standard singlemode fiber (S-SMF) at 820 nm [70] (© 1998 IEEE). **Bottom left:** 12.5 Gbit/s transmission over 100 m MMF and 1 km of 5 μm core diameter SMF at 850 nm [57] (© 1999 IEEE). **Bottom right:** 9 Gbit/s over 100 m GI POF at 830 nm and 7 Gbit/s over 80 m GI POF at 935 nm wavelength [91]

In each part of Fig. 23, we compare the BER at the end of the fiber with back-to-back (b-t-b) measurements. The upper left diagram demonstrates biased as well as bias-free 2.5 Gbit/s data transmission over 500 m MMF (50 μm core diameter) with a nearly singlemode 840 nm VCSEL of 400 μA threshold current, where in the latter case modulation signals with 2 V peak-to-peak

amplitude from a 50 Ω impedance pattern generator are applied [76]. Owing to lower average power consumption and easier driving circuits, bias-free operation might be considered attractive for some applications, but is generally limited by turn-on delay effects. The upper right diagram is 3 Gbit/s biased and 1 Gbit/s bias-free data transmission over 4.3 km of standard SMF with 8.3 µm core diameter [70]. At the emission wavelength of 820 nm, the fiber is operated in a dual-mode guiding regime, so that high order fiber mode filtering had to be applied to overcome intermodal dispersion limitations. Since high-quality 1.3 or 1.55 µm long-wavelength VCSELs are not yet available, the given combination might represent a viable intermediate solution, which is even more easy to implement with 980 nm InGaAs QW based devices due to weaker fiber mode guiding. The lower left diagram displays results of 12.5 Gbit/s data transmission over 100 m MMF with 50 µm core diameter and 1 km of 5 µm diameter SMF with an 850 nm VCSEL [57]. Experiments at the same data rate have also been performed with a 980 nm VCSEL over 1.6 km standard SMF [57], where constraints were imposed by the available fiber length rather than fiber attenuation or dispersion effects. It is seen that MMF power penalties are considerably higher than those for SMF transmission as a result of intermodal dispersion and associated intersymbol interference. Although 10 Gbit/s operation at 980 nm over 500 m of 50 µm MMF has already been demonstrated in 1996 [79], graded-index fibers with bandwidth–length products specifically optimized for 850 nm operation would be beneficial for systems with alignment tolerant power launching and decreased power penalties. Triggered by the work toward a 10-Gigabit Ethernet standard[4] initiated in March 1999, such fibers with 50 µm core diameter and a bandwidth–length product exceeding 2 GHz·km have indeed been developed and have entered the market in the first few months of the year 2000. In [80], 10 Gbit/s data transmission over up to 1.6 km of high-performance MMF incurring less than 3 dB power penalty is reported. A single transverse mode VCSEL emitting at 830 nm was employed to circumvent the chromatic dispersion limit imposed by the high dispersion coefficient that exceeds 100 ps/(km·nm) in the short-wavelength regime. Moreover, this experiment took advantage of a transimpedance amplifier-based and MMF-compatible pin-receiver with close to −18 dBm sensitivity, by which the high optical power levels seen in Fig. 23, largely arising from thermal noise of regular pin-photodiodes, could be overcome. With a longer spool of almost ideal quality fiber, 10 Gbit/s transmission over even 2.8 km was possible [81].

Several options exist to increase the transmission capacity of MMF links. Offset launch from laser into fiber [82], subcarrier multiplexing [83], equalization techniques [84], [85], and multi-level coding [86] all have been successfully applied at Gbit/s data rates, aiming at a better utilization of installed MMFs which show considerable variations of their impulse responses. Similar to long-haul data transmission over singlemode fibers in the 1.55 µm wave-

[4] IEEE 802.3ae, URL http://grouper.ieee.org/groups/802/3/ae/index.html

length window, wavelength division multiplexing (WDM) is another viable option to upgrade a MMF link. However, instead of dense WDM with narrow channel spacing in the 100 GHz regime, coarse WDM systems with several nm spacing to obviate the need for active wavelength stabilization are considered for low-cost MMF links. An integrated coarse WDM module that operates in the 820 to 865 nm wavelength interval and enables 4×2.5 Gbit/s data throughput over 100 m MMF with 62.5 µm core diameter has been demonstrated in [87], whereas 8×155 Mbit/s have been transmitted in the 780 to 860 nm wavelength range over 2 km of 160 MHz·km low-bandwidth MMF in [88]. Even a first 40 Gbit/s system featuring four 815 to 835 nm high-speed singlemode VCSEL channels has been reported in [69], where transmission over 310 m is made possible by a new high-bandwidth MMF.

Much recent progress is observed in plastic optical fiber (POF) data transmission [89], [90]. Especially high-bandwidth graded-index (GI) POFs have the potential to serve as a low cost waveguiding medium for short distance interconnects. The bottom right diagram of Fig. 23 illustrates VCSEL-based data transmission at 9 Gbit/s over 100 m GI POF with 130 µm core diameter at 830 nm and 7 Gbit/s over 80 m GI POF with 155 µm core diameter at 935 nm wavelength [91]. Both fibers are made of perfluorinated material, showing promising attenuation coefficients below 50 dB/km over a wide spectral range, similar to losses of silica glass fibers in their early days. Losses down to 10 dB/km seem to be in close reach, which would help to provide an affordable power budget for eye-safe datacom links with transmission distances in the 100 m range. Although larger diameter POFs offer lower connectorization costs, an obvious challenge for the implementation of high-speed systems is the requirement of similar diameter photodiodes with their associated high capacitance or the need of using high numerical aperture demagnifying optics at the receiver end.

6 Conclusion

The previous discussion has shown that selectively oxidized VCSELs exhibit excellent properties with regard to threshold current, emission spectrum, temperature characteristics, as well as dynamic and noise behavior. The given analysis provides important guidelines for optimizing device performance specifically for applications requiring high-speed modulation. Multimode VCSELs can provide tens of mW output power and can be combined in two-dimensional arrays to generate Watt-level outputs from small-area chips [14], [15]. Continuous-wave operation above 180 °C ambient temperature has been demonstrated, where material dependent gain and carrier loss from the active region are limiting effects. Polarization controlled singlemode devices with side-mode suppression exceeding 30 dB and few-100 µA threshold current show power conversion efficiencies above 30 % in the below-1 mW range of interest for optical interconnection.

Datacom applications of VCSELs exploit the displacement tolerant fiber coupling capabilities and the high modulation current efficiency of the source. Quasi error-free data transmission rates of up to 12.5 Gbit/s over singlemode fiber and silica glass or plastic optical multimode fiber have been obtained using linearly polarized singlemode VCSEL emission. Single frequency devices have been shown to reach the shot noise limit of the relative intensity noise spectrum at mW power level over a frequency range exceeding 10 Gbit/s system requirements.

The results indicate that VCSELs in many respects outperform edge-emitting laser diodes. These devices have already become the dominating transmitter source for commercial high-speed optical interconnects operating in the 800 to 1000 nm wavelength regime, and the emergence of 1.3 and 1.55 μm long-wavelength VCSELs on the market is eagerly awaited.

Acknowledgements

The authors would like to acknowledge support from the German Federal Ministry of Education and Research (BMBF), the German Research Foundation (DFG), the State of Baden-Württemberg, and the European Commission. Special thanks goes to all former and present members of the VCSEL team of Ulm University for many years of successful device and systems research.

References

1. K. Iga, *Fundamentals of Laser Optics.* New York: Plenum Press, 1994.
2. K.J. Ebeling, *Integrated Optoelectronics.* Berlin: Springer, 1993.
3. L.A. Coldren and S.W. Corzine, *Diode Lasers and Photonic Integrated Circuits.* New York: J. Wiley & Sons, 1995.
4. J.L. Jewell, A. Scherer, S.L. McCall, Y.H. Lee, S. Walker, J.P. Harbison, and L.T. Florez, "Low-threshold electrically pumped vertical-cavity surface-emitting microlasers", *Electron. Lett.*, vol. 25, pp. 1123–1124, 1989.
5. R.S. Geels, S.W. Corzine, J.W. Scott, D.B. Young, and L.A. Coldren, "Low threshold planarized vertical-cavity surface-emitting lasers", *IEEE Photon. Technol. Lett.*, vol. 2, pp. 234–236, 1990.
6. M. Orenstein, A.C. Von Lehmen, C. Chang-Hasnain, N.G. Stoffel, J.P. Harbison, L.T. Florez, E. Clausen, and J.E. Jewell, "Vertical-cavity surface-emitting InGaAs/GaAs lasers with planar lateral definition", *Appl. Phys. Lett.*, vol. 56, pp. 2384–2386, 1990.
7. B. Tell, Y.H. Lee, K.F. Brown-Goebeler, J.L. Jewell, R.E. Leibenguth, M.T. Asom, G. Livescu, L. Luther, and V.D. Mattera, "High-power cw vertical-cavity top surface-emitting GaAs quantum well lasers", *Appl. Phys. Lett.*, vol. 57, pp. 1855–1857, 1990.
8. D.L. Huffaker, D.G. Deppe, K. Kumar, and T.J. Rogers, "Native-oxide defined ring contact for low threshold vertical-cavity lasers", *Appl. Phys. Lett.*, vol. 65, pp. 97–99, 1994.

9. R.A. Morgan, J.A. Lehman, and M.K. Hibbs-Brenner, "Vertical-cavity surface-emitting lasers come of age", in *Fabrication, Testing, and Reliability of Semiconductor Lasers*, M. Fallahi and S.C. Wang (Eds.), Proc. SPIE 2683, pp. 18–29, 1996.
10. K.D. Choquette and H.Q. Hou, "Vertical-cavity surface emitting lasers: Moving from research to manufacturing", *Proc. IEEE*, vol. 85, pp. 1730–1739, 1997.
11. K.L. Lear, K.D. Choquette, R.P. Schneider, S.P. Kilcoyne, and K.M. Geib, "Selectively oxidised vertical cavity surface emitting lasers with 50 % power conversion efficiency", *Electron. Lett.*, vol. 31, pp. 208–209, 1995.
12. B. Weigl, M. Grabherr, C. Jung, R. Jäger, G. Reiner, R. Michalzik, D. Sowada, and K.J. Ebeling, "High-performance oxide-confined GaAs VCSELs", *IEEE J. Sel. Top. Quantum Electron.*, vol. 3, pp. 409–415, 1997.
13. D.L. Huffaker, L.A. Graham, H. Deng, and D.G. Deppe, "Sub-40 μA continuous-wave lasing in an oxidized vertical-cavity surface emitting laser with dielectric mirrors", *IEEE Photon. Technol. Lett.*, vol. 8, pp. 974–976, 1996.
14. M. Grabherr, M. Miller, R. Jäger R. Michalzik, U. Martin, H. Unold, and K.J. Ebeling, "High-power VCSEL's: Single devices and densely packed 2-D-arrays", *IEEE J. Sel. Top. Quantum Electron.*, vol. 5, pp. 495–502, 1999.
15. M. Miller, M. Grabherr, R. King, R. Jäger, R. Michalzik, and K.J. Ebeling, "Improved output performance of high-power VCSELs", *IEEE J. Sel. Top. Quantum Electron.*, vol. 7, pp. 210–216, 2001.
16. H.J. Unold, S.W.Z. Mahmoud, R. Jäger, M. Kicherer, M.C. Riedl, and K.J. Ebeling, "Improving single-mode VCSEL performance by introducing a long monolithic cavity", *IEEE Photon. Technol. Lett.*, vol. 10, pp. 939–941, 2000.
17. A. Mooradian, "High brightness cavity-controlled surface emitting GaInAs lasers operating at 980 nm", *Optical Fiber Commun. Conf., OFC*, postdeadline paper PD17. Anaheim, CA, USA, Mar. 2001.
18. M. Kuznetsov, F. Hakimi, R. Sprague, and A. Mooradian, "Design and characteristics of high-power ($>$ 0.5-W CW) diode-pumped vertical-external-cavity surface-emitting semiconductor lasers with circular TEM_{00} beams", *IEEE J. Sel. Top. Quantum Electron.*, vol. 5, pp. 561–573, 1999.
19. S.W. Corzine, R.S. Geels, J.W. Scott, R.-H. Yan, and L.A. Coldren, "Design of Fabry-Perot surface-emitting lasers with a periodic gain structure", *IEEE J. Quantum Electron.*, vol. 25, pp. 1513–1524, 1989.
20. S.W. Corzine, R.H. Yan, and L.A. Coldren, "A tanh substitution technique for the analysis of abrupt and graded interface multilayer dielectric stacks", *IEEE J. Quantum Electron.*, vol. 27, pp. 2086–2090, 1991.
21. P. Yeh, *Optical Waves in Layered Media.* New York: J. Wiley & Sons, 1988.
22. S. Adachi, "GaAs, AlAs, and $\mathrm{Al}_x\mathrm{Ga}_{1-x}\mathrm{As}$: Material parameters for use in research and device applications", *J. Appl. Phys.*, vol. 58, pp. R1–R29, 1985.
23. D.I. Babić and S.W. Corzine, "Analytic expressions for the reflection delay, penetration depth, and absorptance of quarter-wave dielectric mirrors", *IEEE J. Quantum Electron.*, vol. 28, pp. 514–524, 1992.
24. M. Born and E. Wolf, *Principles of Optics*, 6th ed. Oxford: Pergamon Press, 1989.
25. K.J. Ebeling and L.A. Coldren, "Analysis of multielement semiconductor lasers", *J. Appl. Phys.*, vol. 54, pp. 2962–2969, 1983.
26. M. Sugimoto, H. Kosaka, K. Kurihara, I. Ogura, T. Numai, and K. Kasahara, "Very low threshold current density in vertical-cavity surface-emitting laser

diodes with periodically doped distributed Bragg reflectors", *Electron. Lett.*, vol. 28, pp. 385–387, 1992.
27. W. Schmid, D. Wiedenmann, M. Grabherr, R. Jäger, R. Michalzik, and K.J. Ebeling, "CW operation of a diode cascade InGaAs quantum well VCSEL", *Electron. Lett.*, vol. 34, pp. 553–555, 1998.
28. T. Knödl, A. Straub, M. Golling, R. Michalzik, and K.J. Ebeling, "Scaling behavior of bipolar cascade VCSELs", *IEEE Photon. Technol. Lett.*, vol. 13, pp. 930–932, 2001.
29. R. Michalzik and K.J. Ebeling, "Modeling and design of proton-implanted ultralow-threshold vertical-cavity laser diodes", *IEEE J. Quantum Electron.*, vol. 29, pp. 1963–1974, 1993.
30. G. Reiner, E. Zeeb, B. Möller, M. Ries, and K.J. Ebeling, "Optimization of planar Be-doped InGaAs VCSELs with two-sided output", *IEEE Photon. Technol. Lett.*, vol. 7, pp. 730–732, 1995.
31. D. Botez, L.J. Mawst, A. Bhattacharya, J. Lopez, J. Li, T.F. Kuech, V.P. Iakovlev, G.I. Suruceanu, A. Caliman, and A.V. Syrbu, "66 % CW wallplug efficiency from Al-free 0.98 µm-emitting diode lasers", *Electron. Lett.*, vol. 34, pp. 2012–2013, 1996.
32. B. Weigl, M. Grabherr, G. Reiner, and K.J. Ebeling, "High efficiency selectively oxidised MBE grown vertical-cavity surface-emitting lasers", *Electron. Lett.*, vol. 32, pp. 557–558, 1996.
33. R. Michalzik, M. Grabherr, R. Jäger, M. Miller, and K.J. Ebeling, "Progress in high-power VCSELs and arrays", in *Optoelectronic Materials and Devices*, M. Osiński and Y.-K. Su (Eds.), Proc. SPIE 3419, pp. 187–195, 1998.
34. C. Jung, R. Jäger, M. Grabherr, P. Schnitzer, R. Michalzik, B. Weigl, S. Müller, and K.J. Ebeling, "4.8 mW single-mode oxide confined top-surface emitting vertical-cavity laser diodes", *Electron. Lett.*, vol. 33, pp. 1790–1791, 1997.
35. C.J. Chang-Hasnain, J.P. Harbison, C.-E. Zah, M.W. Maeda, L.T. Florez, N.G. Stoffel, and T.-P. Lee, "Multiple wavelength tunable surface-emitting laser arrays", *IEEE J. Quantum Electron.*, vol. 27, pp. 1368–1376, 1991.
36. J. Cheng, P. Zhou, S.Z. Sun, S. Hersee, D.R. Myers, J. Zolper, and G.A. Vawter, "Surface-emitting laser-based smart pixels for two-dimensional optical logic and reconfigurable optical interconnects", *IEEE J. Quantum Electron.*, vol. 29, pp. 741–756, 1993.
37. S.E. Swirhun, R.P. Bryan, W.S. Fu, W.E. Quinn, J.L. Jewell, and G.R. Olbright, "Commercial manufacturing of vertical-cavity surface-emitting laser arrays", in *Vertical-Cavity Surface-Emitting Laser Arrays*, J.L. Jewell (Ed.), Proc. SPIE 2147, pp. 74–84, 1994.
38. S. Matsuo, T. Nakahara, Y. Kohama, Y. Ohiso, S. Fukushima, and T. Kurokawa, "A monolithically integrated smart pixel using an MSM-PD, MESFET's, and a VCSEL", *IEEE J. Sel. Top. Quantum Electron.*, vol. 2, pp. 121–127, 1996.
39. Y. Liu, M. Hibbs-Brenner, B. Morgan, J. Nohava, B. Walterson, T. Marta, S. Bounnak, E. Kalweit, J. Lehman, D. Carlson, and P. Wilson, "Integrated VCSELs, MSM Photodetectors, and GaAs MESFETs for low cost optical interconnects", *OSA Trends in Optics and Photonics*, vol. 15, *Advances in Vertical Cavity Surface Emitting Lasers*, C.J. Chang-Hasnain, ed. (Optical Society of America, Washington, DC 1997), pp. 196–198.

40. H. Kosaka, M. Kajita, M. Yamada, Y. Sugimoto, K. Kurata, T. Tanabe, and Y. Kasukawa, "Plastic-based receptacle-type VCSEL-array modules with one and two dimensions fabricated using the self-alignment mounting technique", in Proc. *47th Electron. Comp. & Technol. Conf., ECTC*, pp. 382–390. San Jose, CA, USA, May 1997.
41. S.Y. Hu, S.Z. Zhang, J. Ko, J.E. Bowers, and L.A. Coldren, "1.5 Gbit/s/channel operation of multiple-wavelength vertical-cavity photonic integrated emitter arrays for low-cost multimode WDM local-area networks", *Electron. Lett.*, vol. 34, pp. 768–770, 1998.
42. R. King, R. Michalzik, D. Wiedenmann, R. Jäger, P. Schnitzer, T. Knödl, and K.J. Ebeling, "2D VCSEL arrays for chip-level optical interconnects", in *Optoelectronic Interconnects VI*, J.P. Bristow and S. Tang (Eds.), Proc. SPIE 3632, pp. 363–372, 1999.
43. R. Michalzik, R. King, R. Jäger, S. Müller, and K.J. Ebeling, "VCSEL arrays for CMOS integrated optical interconnect systems", in *Optoelectronic and Wireless Data Management, Processing, Storage, and Retrieval*, R. Raymond, P.K. Srimani, R. Su, and C.W. Wilmsen (Eds.), Proc. SPIE 4534, pp. 101–113, 2001.
44. J. Piprek, Y.A. Akulova, D.I. Babic, L.A. Coldren, and J.E. Bowers, "Minimum temperature sensitivity of 1.55 μm vertical-cavity lasers at −30 nm gain offset", *Appl. Phys. Lett.*, vol. 72, pp. 1814–1816, 1998.
45. W. Nakwaski and M. Osiński, "Thermal resistance of top-surface-emitting vertical-cavity semiconductor lasers and monolithic two-dimensional arrays", *Electron. Lett.*, vol. 28, pp. 572–574, 1992. Corrected in *Electron. Lett.*, vol. 28, p. 1283, 1992.
46. A.E. Siegman, *Lasers.* Mill Valley: University Science Books, 1986.
47. E. Zeeb, B. Möller, G. Reiner, M. Ries, T. Hackbarth, and K.J. Ebeling, "Planar proton implanted VCSEL's and fiber-coupled 2-D VCSEL arrays", *IEEE J. Sel. Top. Quantum Electron*, vol. 1, pp. 616–623, 1995.
48. M.H. MacDougal, H. Zhao, P.D. Dapkus, M. Ziari, and W.H. Steier, "Wide-bandwidth distributed Bragg reflectors using oxide/GaAs multilayers", *Electron. Lett.*, vol. 30, pp. 1147–1148, 1994.
49. G.R. Hadley, "Effective index model for vertical-cavity surface-emitting lasers", *Opt. Lett.*, vol. 20, pp. 1483–1485, 1995.
50. D. Marcuse, *Light Transmission Optics*, 2nd ed. New York: Van Nostrand Reinhold, 1982.
51. R. Michalzik and K.J. Ebeling, "Generalized BV diagrams for higher order transverse modes in planar vertical-cavity laser diodes", *IEEE J. Quantum Electron.*, vol. 31, pp. 1371–1379, 1995.
52. R. Nagarajan, M. Ishikawa, T. Fukushima, R.S. Geels, and J.E. Bowers, "High speed quantum-well lasers and carrier transport effects", *IEEE J. Quantum Electron.*, vol. 28, pp. 1990–2008, 1992.
53. J.H. Shin, Y.G. Ju, H.E. Shin, and Y.H. Lee, "Spontaneous emission factor of oxidized vertical-cavity surface-emitting lasers from the measured below-threshold cavity loss", *Appl. Phys. Lett.*, vol. 70, pp. 2344–2346, 1997.
54. P.W.A. McIlroy, A. Kurobe, and Y. Uematsu, "Analysis and application of theoretical gain curves to the design of multi-quantum-well lasers", *IEEE J. Quantum Electron.*, vol. 21, pp. 1958–1963, 1985.
55. K.Y. Lau, "Dynamics of quantum well lasers", in P.S. Zory, Jr. (Ed.), *Quantum Well Lasers.* Boston: Academic Press, 1993.

56. R. Olshansky, P. Hill, V. Lanzisera, and W. Powazniak, "Frequency response of 1.3 μm InGaAsP high speed quantum-well semiconductor lasers" *IEEE J. Quantum Electron.*, vol. 23, pp. 1410–1418, 1987.
57. D. Wiedenmann, R. King, C. Jung, R. Jäger, R. Michalzik, P. Schnitzer, M. Kicherer, and K.J. Ebeling, "Design and analysis of single-mode oxidized VCSEL's for high-speed optical interconnects", *IEEE J. Sel. Top. Quantum Electron.*, vol. 5, pp. 503–511, 1999.
58. K.L. Lear, V.M. Hietala, H.Q. Hou, M. Ochiai, J.J. Banas, B.E. Hammons, J.C. Zolper, and S.P. Kilcoyne, "Small and large signal modulation of 850 nm oxide-confined vertical cavity surface emitting lasers", *OSA Trends in Optics and Photonics*, vol. 15, *Advances in Vertical Cavity Surface Emitting Lasers*, C.J. Chang-Hasnain, ed. (Optical Society of America, Washington, DC 1997), pp. 69–74.
59. B.J. Thibeault, K. Bertilsson, E.R. Hegblom, E. Strzelecka, P.D. Floyd, R. Naone, and L.A. Coldren, "High-speed characteristics of low-optical loss oxide-apertured vertical-cavity lasers", *IEEE Photon. Technol. Lett.*, vol. 9, pp. 11–13, 1997.
60. K. Petermann, *Laser Diode Modulation and Noise*. Dordrecht: Kluwer Academic Publishers, 1991.
61. D.C. Kilper, P.A. Roos, J.L. Carlsen, and K.L. Lear, "Squeezed light generated by a microcavity laser", *Phys. Rev. A*, vol. 55, pp. 3323–3326, 1997.
62. D. Wiedenmann, P. Schnitzer, C. Jung, M. Grabherr, R. Jäger, R. Michalzik, and K.J. Ebeling, "Noise characteristics of 850 nm single-mode vertical cavity surface emitting lasers", *Appl. Phys. Lett.*, vol. 73, pp. 717–719, 1998.
63. C.H. Henry, "Phase noise in semiconductor lasers", *J. Lightwave Technol.*, vol. 4, pp. 298–311, 1986.
64. W. Schmid, C. Jung, B. Weigl, G. Reiner, R. Michalzik, and K.J. Ebeling, "Delayed self-heterodyne linewidth measurement of VCSEL's", *IEEE Photon. Technol. Lett.*, vol. 8, pp. 1288–1290, 1996.
65. H.P. Zappe, F. Monti di Sopra, H.-P. Gauggel, K. Gulden, R. Hövel, and M. Moser, "High-spectral-purity VCSELs for spectroscopy and sensors", in *Laser Diodes and LEDs in Industrial, Measurement, Imaging, and Sensors Applications II*, G.T. Burnham, X. He, K.J. Linden, and S.C. Wang (Eds.), Proc. SPIE 3945, pp. 106–116, 2000.
66. G.P. Agrawal, *Fiber-Optic Communication Systems*, 2nd ed. New York: J. Wiley & Sons, 1997.
67. K. Drögemüller, D. Kuhl, J. Blank, M. Ehlert, T. Kraeker, J. Höhn, D. Klix, V. Plickert, L. Melchior, I. Schmale, P. Hildebrandt, M. Heinemann, F.P. Schiefelbein, L. Leininger, H.-D. Wolf, T. Wipiejewski, and A. Ebberg, "Current progress of advanced high speed parallel optical links for computer clusters and switching systems", in Proc. *50th Electron. Comp. & Technol. Conf., ECTC*, pp. 1227–1235. Las Vegas, NV, USA, May 2000.
68. R. Michalzik, K.J. Ebeling, M. Kicherer, F. Mederer, R. King, H. Unold, and R. Jäger, "High-performance VCSELs for optical data links", *IEICE Trans. Electron.*, vol. E84-C, pp. 629–638, 2001. Also published in *IEICE Trans. Commun.*, vol. E84-B, pp. 1255–1264, 2001.
69. R. Michalzik, G. Giaretta, K.W. Goossen, J.A. Walker, and M.C. Nuss, "40 Gb/s coarse WDM data transmission with 825 nm wavelength VCSELs over 310 m of high-performance multimode fiber", in Proc. *26th Europ. Conf. on Opt. Commun., ECOC*, vol. 4, pp. 33–34. Munich, Germany, Sept. 2000.

70. P. Schnitzer, R. Jäger, C. Jung, R. Michalzik, D. Wiedenmann, F. Mederer, and K.J. Ebeling, "Biased and bias-free multi-Gb/s data links using GaAs VCSEL's and 1300-nm single-mode fiber", *IEEE Photon. Technol. Lett.*, vol. 10, pp. 1781–1783, 1998.
71. U. Fiedler and K.J. Ebeling, "Design of VCSELs for feedback insensitive data transmisson and external cavity mode-locking", *IEEE J. Sel. Top. Quantum Electron.*, vol. 1, pp. 442–450, 1995.
72. D. Wiedenmann, M. Grabherr, C. Jung, R. Jäger, R. Michalzik, P. Schnitzer, and K.J. Ebeling, "Feedback insensitive 3 Gb/s fiber interconnect with low noise single-mode VCSEL", in Proc. *24th Europ. Conf. on Opt. Commun., ECOC*, vol. 1, pp. 457–458. Madrid, Spain, Sept. 1998.
73. K.J. Ebeling, "Optical interconnects and data links with vertical cavity surface emitting laser diodes (VCSEL)", in Proc. *21st Europ. Conf. on Opt. Commun., ECOC*, vol. 4, pp. 113–147. Brussels, Belgium, Sept. 1995.
74. J. Heinrich, E. Zeeb, and K.J. Ebeling, "Transverse modes under external feedback and fiber coupling efficiencies of VCSEL's", *IEEE Photon. Technol. Lett.*, vol. 10, pp. 1365–1367, 1998.
75. R. Michalzik, P. Schnitzer, U. Fiedler, D. Wiedenmann, and K.J. Ebeling, "High-bit-rate data transmission with short-wavelength oxidized VCSEL's: Toward bias-free operation", *IEEE J. Sel. Top. Quantum Electron.*, vol. 3, pp. 396–404, 1997.
76. P. Schnitzer, M. Grabherr, R. Jäger, C. Jung, and K.J. Ebeling, "Bias-free 2.5 Gbit/s data transmission using polyimide passivated GaAs VCSELs", *Electron. Lett.*, vol. 34, pp. 573–575, 1998.
77. K.H. Hahn, M.R. Tan, Y.M. Houng, and S.Y. Wang, "Large area multitransverse-mode VCSELs for modal noise reduction in multimode fibre systems", *Electron. Lett.*, vol. 29, pp. 1482–1484, 1993.
78. D.M. Kuchta and C.J. Mahon, "Mode selective loss penalties in VCSEL optical fiber transmission links", *IEEE Photon. Technol. Lett.*, vol. 6, pp. 288–290, 1994.
79. U. Fiedler, G. Reiner, P. Schnitzer, and K.J. Ebeling, "Top-surface emitting vertical-cavity laser diodes for 10 Gbit/s data transmission", *IEEE Photon. Technol. Lett.*, vol. 8, pp. 746–748, 1996.
80. R. Michalzik, G. Giaretta, A.J. Ritger, and Q.L. Williams, "10 Gb/s VCSEL based data transmission over 1.6 km of new generation 850 nm multimode fiber", *IEEE Lasers and Electro-Opt. Soc. Ann. Meet., LEOS*, postdeadline paper PD1.6. San Francisco, CA, USA, Nov. 1999.
81. G. Giaretta, R. Michalzik, and A.J. Ritger, "Long distance (2.8 km), short wavelength (0.85 μm) data transmission at 10 Gb/sec over new generation high bandwidth multimode fiber", *Conf. on Lasers and Electro-Opt., CLEO*, postdeadline paper CPD13. San Francisco, CA, USA, May 2000.
82. L. Raddatz, I.H. White, D.G. Cunningham, and M.C. Novell, "An experimental and theoretical study of the offset launch technique for the enhancement of the bandwidth of multimode fiber links", *J. Lightwave Technol.*, vol. 16, pp. 324–331, 1998.
83. T.K. Woodward, S. Hunsche, A.J. Ritger, and J.B. Stark, "1-Gb/s BPSK transmission at 850 nm over 1 km of 62.5-µm-core multimode fiber using a single 2.5-GHz subcarrier", *IEEE Photon. Technol. Lett.*, vol. 11, pp. 382–384, 1999.

84. M. Bruensteiner, G.C. Papen, J. Poulton, S. Tell, R. Palmer, K. Giboney, D. Dolfi, and S. Corzine, "3.3-V CMOS pre-equalization VCSEL transmitter for gigabit multimode fiber links", *IEEE Photon. Technol. Lett.*, vol. 11, pp. 1301–1303, 1999.
85. X. Zhao and F.-S. Choa, "10 Gb/s multimode fiber transmissions over any (loss-limited) distances using adaptive equalization techniques", in Proc. *26th Europ. Conf. on Opt. Commun., ECOC*, vol. 3, pp. 57–58. Munich, Germany, Sept. 2000.
86. I.H. White, M. Webster, and R.V. Penty, "High bandwidth optical links over multimode fibre", in Proc. *IEEE Lasers and Electro-Opt. Soc. Ann. Meet., LEOS*, vol. 2, pp. 695–696. San Francisco, CA, USA, Nov. 1999.
87. L.B. Aronson, B.E. Lemoff, L.A. Buckman, and D.W. Dolfi, "Low-cost multimode WDM for local area networks up to 10 Gb/s", *IEEE Photon. Technol. Lett.*, vol. 10, pp. 1489–1491, 1998.
88. E.B. Grann, K. Herrity, B.C. Peters, and B. Wiedemann, "Datacom applications for new VCSEL technologies", in *Vertical-Cavity Surface-Emitting Lasers IV*, K.D. Choquette and C. Lei (Eds.), Proc. SPIE 3946, pp. 165–169, 2000.
89. See, e.g., papers in Proc. *7th Int.'l Plastic Optical Fibres Conf., POF '98.* Berlin, Germany, Oct. 1998; Proc. *8th Int.'l POF Conf.* Makuhari Messe, Chiba, Japan, July 1999; Proc. *The Int.'l POF Technical Conf.* Cambridge, MA, USA, Sept. 2000; Proc. *10th Int.'l Plastic Optical Fibres Conf. 2001.* Amsterdam, The Netherlands, Sept. 2001.
90. R. Michalzik, "Optical Backplanes, Board and Chip Interconnects", in C. DeCusatis (Ed.), *Fiber Optic Data Communication: Technological Trends and Advances*, pp. 216–269. San Diego: Academic Press, 2002.
91. G. Giaretta, F. Mederer, R. Michalzik, W. White, R. Jäger, G. Shevchuk, T. Onishi, M. Naritomi, R. Yoshida, P. Schnitzer, H. Unold, M. Kicherer, K. Al-Hemyari, J.A. Valdmanis, M. Nuss, X. Quan, and K.J. Ebeling, "Demonstration of 500 nm-wide transmission window at multi-Gb/s data rates in low-loss plastic optical fiber", in Proc. *25th Europ. Conf. on Opt. Commun., ECOC*, vol. II, pp. 240–241. Nice, France, Sept. 1999.